Marine Boundary Layers above Heterogeneous SST: Alongfront Winds

PETER P. SULLIVAN,[a] JAMES C. MCWILLIAMS,[b] JEFFREY C. WEIL,[a] EDWARD G. PATTON,[a] AND
HARINDRA J. S. FERNANDO[c]

[a] *National Center for Atmospheric Research, Boulder, Colorado*
[b] *Department of Atmospheric and Oceanic Sciences, University of California, Los Angeles, Los Angeles, California*
[c] *Department of Civil and Environmental Engineering and Earth Sciences, University of Notre Dame, South Bend, Indiana*

(Manuscript received 12 March 2021, in final form 9 June 2021)

ABSTRACT: Turbulent flow in a weakly convective marine atmospheric boundary layer (MABL) driven by geostrophic winds $V_g = 10\,\mathrm{m\,s^{-1}}$ and heterogeneous sea surface temperature (SST) is examined using fine-mesh large-eddy simulation (LES). The imposed SST heterogeneity is a single-sided warm or cold front with jumps $\Delta\theta = (2, -1.5)$ K varying over a horizontal x distance of 1 km characteristic of an upper-ocean mesoscale or submesoscale front. The geostrophic winds are oriented parallel to the SST isotherms (i.e., the winds are alongfront). Previously, Sullivan et al. examined a similar flow configuration but with geostrophic winds oriented perpendicular to the imposed SST isotherms (i.e., the winds were across-front). Results with alongfront and across-front winds differ in important ways. With alongfront winds, the ageostrophic surface wind is weak, about 5 times smaller than the geostrophic wind, and horizontal pressure gradients couple the SST front and the atmosphere in the momentum budget. With across-front winds, horizontal pressure gradients are weak and mean horizontal advection primarily balances vertical flux divergence. Alongfront winds generate persistent secondary circulations (SC) that modify the surface fluxes as well as turbulent fluxes in the MABL interior depending on the sign of $\Delta\theta$. Warm and cold filaments develop opposing pairs of SC with a central upwelling or downwelling region between the cells. Cold filaments reduce the entrainment near the boundary layer top that can potentially impact cloud initiation. The surface-wind–SST-isotherm orientation is an important component of atmosphere–ocean coupling. The results also show frontogenetic tendencies in the MABL.

KEYWORDS: Atmosphere-ocean interaction; Fluxes; Small scale processes; Turbulence; Large eddy simulations

1. Introduction

It is now widely recognized that the ocean surface is spatially heterogeneous at a wide range of scales under the action of submesoscale ocean turbulence and larger-scale ocean eddies (McWilliams 2016). Mesoscale and submesoscale motions generate long-lived horizontal gradients in the surface temperature, buoyancy and currents, and ongoing research seeks to understand how the broadband dynamics and heterogeneity of the ocean surface couple to the overlying marine atmospheric boundary layer (Chelton et al. 2004; Seo et al. 2016; Renault et al. 2019; Skyllingstad et al. 2019), to sea breezes (Miller et al. 2003; Wang et al. 2018), to clouds (Atkinson and Zhang 1996; Stevens et al. 2021), and ultimately to the larger-scale atmospheric motions impacting weather and climate (Small et al. 2008; Wijesekera et al. 2016; Quinn et al. 2021; Shroyer et al. 2021). The current and thermal coupling pathways between the ocean surface and the overlying boundary layer are abundant (Edson et al. 2007; Sullivan and McWilliams 2010; D'Asaro 2014; Cronin et al. 2019; Liang et al. 2020). In the present work we focus on thermal coupling and the impact of variable sea surface temperature (SST) on the marine atmospheric boundary layer (MABL).

In previous work, Sullivan et al. (2020, hereafter S20) examined the impact of heterogeneous one-sided warm and cold SST fronts of varying scale [0.1–6] km on weakly convective boundary layer dynamics. The process studies were carried out using large-eddy simulations (LES) on fine meshes in large horizontal domains driven by large-scale geostrophic winds blowing perpendicular to the imposed SST isotherms, i.e., a geostrophic wind–SST regime we referred to as "across-front winds." A Fourier-fringe technique was implemented in the LES to overcome the assumptions of horizontally homogeneous periodic flow. Across-front winds were found to generate secondary circulations (SC) that vary with the sign of the front. Somewhat unexpected, warm fronts feature a superadiabatic surface layer, nonlinear temperature and momentum flux profiles, a local maximum in the vertical velocity variance, and an extended spatial evolution of the boundary layer with increasing distance from the SST front. Cold fronts collapse the incoming turbulence but leave behind residual motions above the boundary layer. In the case of a warm front, the internal boundary layer grows with downstream distance conveying the surface changes aloft and downwind. SST fronts modify entrainment fluxes and generate persistent horizontal advection at large distances from the front.

The present work examines a 90° rotation in the wind–SST heterogeneity orientation focusing on atmospheric boundary layers driven by large-scale geostrophic winds blowing parallel to SST isotherms, i.e., a regime we refer to as "alongfront winds." Heterogeneous boundary layers driven by alongfront winds are much less studied compared to their across-front wind counterparts; a notable exception is Wenegrat and Arthur (2018) that examined horizontally periodic changes in SST on the MABL. With alongfront winds, Coriolis forces

---

Corresponding author: Peter P. Sullivan, pps@ucar.edu

DOI: 10.1175/JAS-D-21-0072.1

generate ageostrophic winds, a wind shear, oriented perpendicular to the SST isotherms, which are an order of magnitude smaller than the geostrophic wind (e.g., Wyngaard 2010); thus ageostrophic advection is also weaker with alongfront winds. Adopting the ageostrophic wind as a velocity scale the alongfront wind regime is then a distant cousin to convective boundary layers driven by temperature flux with zero mean wind, i.e., free convection (e.g., Schmidt and Schumann 1989). There is a large body of prior work examining the impact of surface heterogeneity on land boundary layers in free convection; for simplicity turbulence simulations of this boundary layer regime almost universally adopt periodic sidewalls. Results find surface heterogeneity acts to organize the updraft and downdraft patterns of the thermal plumes; the updrafts and downdrafts are connected by internal SC (e.g., Krettenauer and Schumann 1992; Raasch and Harbusch 2001; Patton et al. 2005). We note wind shear direction is important even in homogeneous convective boundary layers as it tends to orient the central axis of the large-scale coherent structures (e.g., Sykes and Henn 1989; Moeng and Sullivan 1994), and wind shear direction is also important in 2D closure modeling of convective boundary layers (Lilly 1986; Moeng et al. 2004). Also Anderson et al. (2015) finds secondary circulations are generated in a neutral boundary layer with heterogeneous strip roughness oriented parallel to the main flow direction because of oscillations in turbulence production in the roughness sublayer.

In contrast to the MABL, the impact of alongfront surface winds on upper-ocean mixing remains one of the most commonly studied canonical regimes; the ageostrophic currents that develop with alongfront surface winds can impact the frontogenetic dynamics of density filaments and fronts also because of secondary circulations (e.g., Thomas and Lee 2005; Taylor and Ferrari 2010; McWilliams et al. 2015; Sullivan and McWilliams 2018, 2019; McWilliams 2020). Taken together, the available evidence in the atmospheric and upper-ocean boundary layers hint at a possible importance of wind shear direction and the formation of secondary circulations in the presence of SST surface heterogeneity under large geostrophic winds.

The outline of the paper is as follows: the LES equations appropriate for a high-Reynolds-number heterogeneous MABL introduced in S20 are presented in section 2 and the suite of LES experiments is described in section 3. Results and comparison with S20 are discussed in section 4, and section 5 provides a summary and discussion of the findings.

2. LES governing equations

The LES equations and solution algorithm are briefly described in order to introduce the coordinate system and variables used in the simulations and analysis, see Fig. 1. The following notation is used: $\mathbf{u} \equiv u_i = (u, v, w)$ denote the Cartesian velocity components, θ is virtual potential temperature and p is the pressure variable normalized by density ρ. The three Cartesian coordinates are $\mathbf{x} \equiv x_i = (x, y, z)$ are also referred to as (zonal, meridional, vertical) directions, respectively. The set of LES equations that describe rotating stratified turbulent flow in a MABL under the incompressible Boussinesq approximation are as follows:

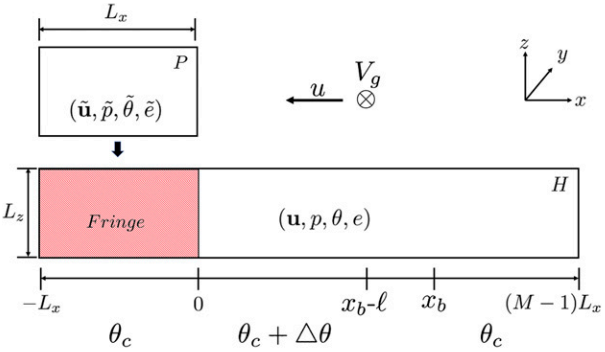

FIG. 1. Sketch of periodic P and heterogeneous H LES domains used to simulate a spatially developing nonperiodic marine atmospheric boundary layer driven by positive-signed geostrophic winds V_g (the tail of the vector is into the page). Then the nominal ageostrophic wind u is flowing from right to left in the sketch. The size of the domains is (L_x, L_y, L_z) and (ML_x, L_y, L_z) with $M = 10$. The field variables in P are denoted $(\tilde{\mathbf{u}}, \tilde{p}, \tilde{\theta}, \tilde{e})$ and in H are denoted $(\mathbf{u}, p, \theta, e)$. In domain P the imposed surface temperature is θ_c. In H the surface temperature is heterogeneous: θ_c is incremented by $\Delta\theta$ over a distance $\ell = 1000$ m starting at the break point $x_b \sim 18.6$ km, see Eq. (3).

$$\frac{\partial \mathbf{u}}{\partial t} = -\mathbf{u} \cdot \nabla \mathbf{u} - \mathbf{f} \times (\mathbf{u} - \mathbf{U}_g) - \nabla p + \mathbf{z}\beta(\theta - \theta_o) - \nabla \cdot \mathbf{T}, \quad (1a)$$

$$\frac{\partial \theta}{\partial t} = -\mathbf{u} \cdot \nabla \theta - \nabla \cdot \mathbf{B}, \quad (1b)$$

$$\frac{\partial e}{\partial t} = -\mathbf{u} \cdot \nabla e + \mathcal{P} + \mathcal{B} + \mathcal{D} - \mathcal{E}, \quad (1c)$$

$$\nabla \cdot \mathbf{u} = 0. \quad (1d)$$

The above equation set includes transport equations: for momentum $\rho\mathbf{u}$ (1a); for virtual potential temperature θ (1b); and for SGS turbulent kinetic energy e (1c). The divergence-free (incompressible) condition (1d) determines the elliptic pressure variable p. Equation set (1) also includes: geostrophic winds $\mathbf{U}_g = (U_g, V_g)$, rotation vector $\mathbf{f} = (0, 0, f)$ with Coriolis parameter f, unit vector $\mathbf{z}$ in the vertical direction, and buoyancy parameter $\beta = g/\theta_o$, where g is gravity and θ_o is the reference potential temperature. The SGS momentum and temperature fluxes $(\mathbf{B}, \mathbf{T})$ are estimated using turbulent eddy viscosity prescriptions $(\nu_t, \nu_\theta) \sim \sqrt{e}$, where e is SGS turbulent kinetic energy. The transport equation, Eq. (1d), for SGS e contains a standard set of right-hand-side terms: production $\mathcal{P}$, buoyancy $\mathcal{B}$, diffusion $\mathcal{D}$, and viscous dissipation $\mathcal{E}$, which are modeled using the formulas summarized in Sullivan et al. (1994) and Moeng and Sullivan (2015). To streamline the notation we omit the standard overbar notation $\overline{()}$ indicating LES spatial filtering in (1), and also simply refer to virtual potential temperature θ as "temperature."

At the lower boundary we impose rough wall boundary conditions based on bulk aerodynamic formulas where the transfer coefficients are determined from Monin–Obukhov (MO) similarity functions (Moeng 1984). The MO rules are applied point-by-point at the lower boundary as described in S20. The SST heterogeneity varies only in the x direction and thus the flow is assumed to be periodic in the y direction. In the x direction the inflow and outflow to the computational domain is controlled by a numerical Fourier-fringe method described in section 3a. The Fourier-fringe method (Spalart and Watmuff 1993; Nordström et al. 1999): 1) is a general recipe for simulating nonperiodic spatially developing turbulent boundary layers in finite domains; 2) permits the use of standard Fourier transforms; 3) does not require separate artificial boundary conditions; and 4) generates stratified boundary layer turbulence with realistic coherent structures that flow over the SST fronts as shown in S20.

We utilize well-established algorithms to integrate the LES equations, Eqs. (1). The equations are advanced in time using an explicit fractional step method that enforces incompressibility at every stage of the third-order Runge–Kutta (RK3) scheme. Dynamic time stepping with a fixed Courant–Friedrichs–Lewy (CFL) is used. The spatial discretization is second-order finite difference in the vertical direction and pseudospectral in the x and y directions. Further algorithmic details are given by Moeng (1984), Sullivan et al. (1994, 1996), McWilliams et al. (1999), Sullivan and Patton (2011), Moeng and Sullivan (2015), and the references cited therein.

3. LES details and experiments

The design and numerical implementation of the LES experiments follows the recipe outlined in S20 with the important differences mentioned below. In the present study, we examine the impact of heterogeneous SST on the marine atmospheric boundary layer with geostrophic winds $\mathbf{U}_g = (0, V_g)$ oriented parallel to the SST isotherms, i.e., an alongfront wind configuration. The geostrophic wind $V_g = 10\,\mathrm{m\,s^{-1}}$, the Coriolis parameter $f = 10^{-4}\,\mathrm{s^{-1}}$, and the roughness $z_o = 2 \times 10^{-4}\,\mathrm{m}$ is picked to be representative of a wavy ocean surface based on winds $\leq 10\,\mathrm{m\,s^{-1}}$ (Large and Pond 1981). For our process studies, the imposed SST heterogeneity is time invariant, varies solely in the x direction, and has single-sided SST fronts with a jump between two temperature levels over a finite x distance. In S20 the geostrophic wind $U_g = 10\,\mathrm{m\,s^{-1}}$ was oriented perpendicular to the SST isotherms, i.e., an across-front wind configuration. Although the present simulation design targets an MABL with small surface roughness and strip thermal heterogeneity, the background conditions can be easily modified for atmospheric boundary layers developing over heterogeneous landscapes.

a. Fourier-fringe scheme with alongfront winds

Our implementation of the Fourier-fringe scheme utilizes two computational domains P and H as shown in Fig. 1. Notice a separate finite length fringe domain is attached to the primary computational domain H. Turbulent flow in the small LES domain P is horizontally homogeneous and sets the inflow-outflow conditions in the large LES domain H that contains heterogeneous SST. To distinguish flow variables in the different domains, variables in the P domain are indicated by an overtilde, e.g., $\tilde{\mathbf{u}}$. In the fringe region of H, the red colored area in Fig. 1, fringe forces are added to the right-hand side of the LES equations that effectively nudge the fields in H to match their counterparts in P. In (1), the added forces take the following form:

$$\frac{\partial \mathbf{u}}{\partial t} = \cdots + A\lambda(x)(\tilde{\mathbf{u}} - \mathbf{u}), \tag{2a}$$

$$\frac{\partial \theta}{\partial t} = \cdots + A\lambda(x)(\tilde{\theta} - \theta), \tag{2b}$$

$$\frac{\partial e}{\partial t} = \cdots + A\lambda(x)(\tilde{e} - e). \tag{2c}$$

The ellipses in (2) denote the complete right hand side of the LES equations, Eqs. (1), and the added forces depend on the instantaneous pointwise difference between the fields in P and H. The weighting function $\lambda(x)$ varies smoothly with x and is scaled by the inverse time scale $A = 5\,\mathrm{s^{-1}}$; outside the fringe region $\lambda(x) = 0$, see Eq. (3) in S20. In our fractional-step Runge–Kutta time stepping scheme the fringe forces are added prior to the pressure update. The nudging is strong and forces the turbulent inflow in H to match the turbulent flow in P. We mention that the fringe scheme used here can be generalized for arbitrary wind directions with surface heterogeneity in two directions by running two fully overlapping LES domains P and H. Then the fringe region is located on all four sides of the horizontal domain H, but of course this doubles the computational time.

b. LES domains

The particulars of the two LES domains in Fig. 1 are as follows: domain P is $(L_x, L_y, L_z) = (3.375, 3.375, 1.4)$ km and is discretized with a grid mesh $(N_x, N_y, N_z) = (768, 768, 384)$ grid points. Domain H is $(10L_x, L_y, L_z) = (33.75, 3.375, 1.4)$ km and is discretized with a grid mesh $(10N_x, N_y, N_z) = (7680, 768, 384)$ grid points. In H the origin of the x axis is at the right edge of the fringe region. In both domains the horizontal spacing is constant $\Delta x = \Delta y = 4.4$ m, while the spacing between grid points Δz in the vertical mesh is smoothly varying using the constant stretching factor $K = \Delta z_{i+1}/\Delta z_i = 1.002\,88$; the first w-grid level $z_1 = 2$ m.

In S20 with across-front geostrophic winds we picked the location of the break point x_b where the SST starts to change relatively near the right edge of the fringe region $x_b = 2.7$ km: this allowed the perturbed boundary layer to spatially develop over a considerable downstream distance approaching 30 km. In the present study with alongfront geostrophic winds we choose x_b based on the expected development of the much weaker ageostrophic Ekman flow. Recall under homogeneous conditions Ekman dynamics result in surface winds rotated counterclockwise i.e., to the left of the geostrophic wind direction (e.g., Wyngaard 2010). Thus, with $(V_g, f) > 0$ the ageostrophic wind $u(z) < 0$ and flows from right-to-left across the SST front as shown in Fig. 1. Then the (inflow, outflow) in domain H are located at $x = [9L_x, 0]$, respectively. Fourier derivatives in the x direction are evaluated on the interval $x = [-L_x, 9L_x]$. With this setup, preliminary runs on coarse grids

TABLE 1. SST variations in the heterogeneous H domain with alongfront winds; see Fig. 1.

Case	ℓ (km)	$\Delta\theta$ (K)	$(x_b - \ell, x_b)$ (km)
Nu1	1	2	(17.56, 18.56)
Ns1	1	−1.5	(17.56, 18.56)

generated a complex set of secondary circulations to the left of the imposed SST change, i.e., between $0 < x < x_b$. Thus, to allow sufficient spatial evolution of the boundary layer with alongfront winds we locate the breakpoint x_b near the middle of domain H.

In domain H (see Fig. 1), the distribution of sea surface temperature θ_s for a single one-sided front is given by the rule:

$$\theta_s(x) = \begin{cases} \theta_c: & -L_x < x < 0 \\ \theta_c + \Delta\theta: & 0 < x < x_b - l \\ \theta_c + \dfrac{\Delta\theta}{l}(x_b - x): & x_b - l < x < x_b \\ \theta_c: & x_b < x \end{cases} . \tag{3}$$

The constant $\theta_c = 290.17$ K, $\Delta\theta$ is the magnitude of the SST jump over the length scale ℓ, and $x_b = 5.5L_x = 18\,562.5$ m marks the start of the jump. As in S20 negative and positive horizontal gradients in SST are created by setting $\Delta\theta = (2, -1.5)$ K with $\ell = 1$ km. Based on the sign of the ageostrophic wind we refer to (positive, negative) $\Delta\theta$ jumps as warm and cold front cases (Nu1, Ns1), respectively; simulation details are provided in Table 1. The geostrophic wind and surface roughness in P are set to values in the H domain, while the SST in P is set equal to the constant value $\theta_s = \theta_c$.

A special recipe is used to build the initial conditions for the simulations in H. First, the LES in domain P is run independently with an unstable surface temperature flux $Q_* = 0.015$ K m s^{-1}($\sim$15 W m^{-2}) and $V_g = 10$ m s^{-1}. The initial stratification profile is two linear segments, $\theta = \theta_c$ for $0 < z < \tilde{z}_i$ and $\theta = \theta_c + (z - \tilde{z}_i)\,\partial_z\theta$ for $z > \tilde{z}_i$. The initial state is $\theta_c = 290$ K, $\tilde{z}_i = 250$ m and $\partial_z\theta = 0.003$ K m^{-1}. The integration time for the spinup is approximately 6500 s which is sufficient to generate fully developed stratified turbulence typical of a weakly unstable MABL (Sullivan et al. 2014, and S20). The last data volume from the P simulation is archived, replicated M times, and serves as the initial condition for simulations in H. This initialization recipe is inexpensive and provides a high-quality first estimate of the flow state in the H domain. Finally, the LES is restarted but now with θ_s given by (3) as the surface boundary condition. The simulations in P and H run concurrently with one-way coupling from P to H in the fringe region using (2). The simulations are run for 16 900 s requiring ~90 000 time steps. Based on the convective velocity scale and boundary layer depth in Table 2 this integration time is ~16 large-eddy turnover times. We examined the solutions for varying time and found that the restart generates a transient pulse which propagates through the stratified flow in the LES domain (e.g., Manasseh et al. 1998). The statistics presented here are collected over the last 5400 s of the simulation after the pulse has faded away; the time averaging is approximately 5.4 large-eddy turnover times when the statistics are quasi-steady.

c. *Averaging*

In the H domain, the spatial inhomogeneity in the x direction complicates the analysis of the LES solutions. To diagnose mean and turbulence fields in statistics and flow visualization we use a combination of temporal and spatial averaging. At any time step in the simulation we project the flow fields onto an x–z plane by spatial averaging in the alongfront or homogeneous y direction; this generates an x–z plane of data for each statistic, e.g., an average of the temperature field $\overline{\theta}(x, z) = \int_y \theta(x, y, z)\,dy$. The x–z planes of data are sampled at fine time resolution in the LES and are archived for further processing. Robust statistics are generated from the the x–z data planes by first computing a running average in x using a window of width 850 m followed by a time average over the last 5400 s of the simulation. This suite of space and time averaging operations is indicated by angle brackets $\langle\,\rangle$ in the narrative.

Any variable ϕ in the H domain is decomposed into a mean $\langle\phi\rangle$, that varies with (x, z) and fluctuation ϕ' by

$$\phi'(\mathbf{x}) = \phi(\mathbf{x}) - \langle\phi\rangle(x, z)\,. \tag{4}$$

Products of flow variables, as well as terms in the momentum and temperature budgets, are constructed using (4). To compute, for example, average vertical fluxes and variances of turbulence we use the following identities:

$$\langle\phi' w'\rangle = \langle\phi w\rangle - \langle\phi\rangle\langle w\rangle \quad \text{and} \quad \langle\phi'\phi'\rangle = \langle\phi\phi\rangle - \langle\phi\rangle\langle\phi\rangle\,. \tag{5}$$

Numerous statistical moments are computed including means, resolved variances, vertical and horizontal fluxes, SGS fluxes and energy, pressure, and the third moment of resolved vertical velocity.

d. *Normalization*

We use surface-layer statistics, wind and temperature profiles, and boundary layer depth computed near the right inflow

TABLE 2. Bulk boundary layer properties with alongfront (north) winds and across-front (east) winds from S20; the prefix N and E indicates north and east, respectively.

Case	(U_g, V_g) (m s^{-1})	$\hat{u}_*$ (m s^{-1})	$\hat{Q}_*$ (K m s^{-1})	$\hat{w}_*$ (m s^{-1})	$\hat{z}_i$ (m)	$-\hat{L}$ (m)	$-\hat{z}_i/\hat{L}$ (–)	$\hat{z}_i/\ell$ (–)
Nu1	(0, 10)	0.285	0.0098	0.601	656	174	3.77	0.656
Ns1	(0, 10)	0.283	0.0099	0.602	652	169	3.85	0.652
Eu2	(10, 0)	0.286	0.0115	0.602	560	150	3.74	0.560
Es2	(10, 0)	0.286	0.0115	0.602	560	150	3.74	0.560

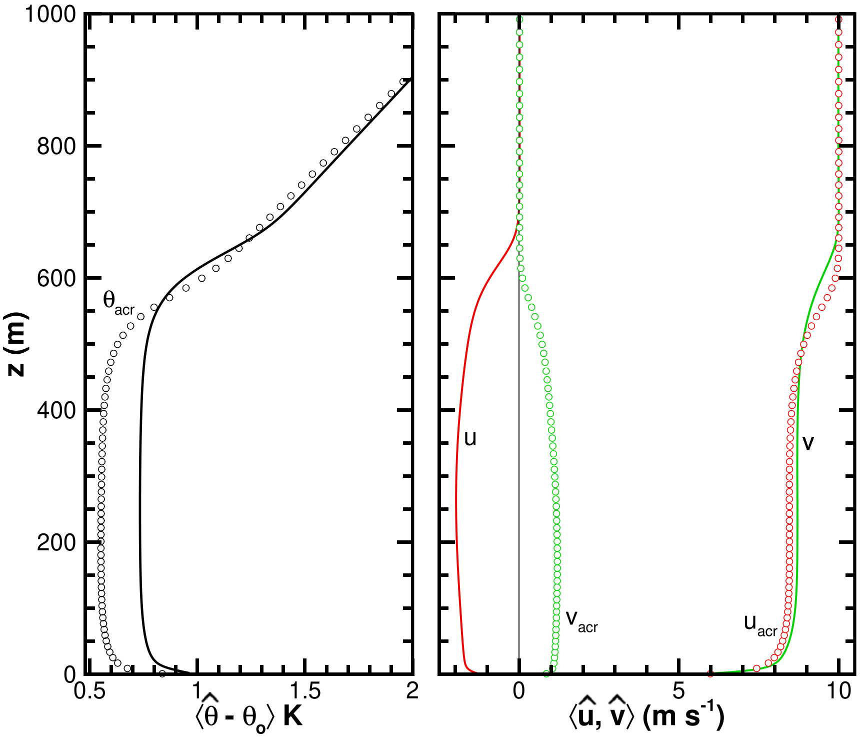

FIG. 2. Profiles of the (left) mean temperature $\hat{\theta}$ and (right) wind components $\langle \hat{u}, \hat{v} \rangle$ in the far field $x \sim 30$ km with alongfront geostrophic winds. For comparison, the vertical profiles from the simulation with across-front geostrophic winds from S20 are shown as open circles with a subscript "acr"; these mean winds $\langle \hat{u}_{\rm acr}, \hat{v}_{\rm acr} \rangle$ are indicated by red and green colors, respectively. Note that $|\hat{u}| < |\hat{u}_{\rm acr}|$ for the same magnitude of geostrophic wind forcing. The boundary layer with alongfront geostrophic winds is run longer in time producing a deeper and warmer boundary layer than in S20.

boundary of the H domain for normalization and as reference for comparison with fields in the interior of the H domain; turbulence near the right inflow boundary is referred to as the "far field" with far-field statistics denoted by an overhat, e.g., $\langle \hat{\mathbf{u}} \rangle$. Section 4a shows that the turbulence near the right inflow boundary is in good agreement with turbulent flow in a similarly forced horizontally homogeneous MABL. Table 2 is a compilation of computed bulk statistics in the far field, viz., friction velocity $\widehat{u_*}$, temperature flux $\widehat{Q_*}$, convective velocity scale $\widehat{w_*}$, boundary layer depth $\widehat{z_i}$ (Sullivan et al. 1998) and S20, stability parameter $\widehat{z_i}/\hat{L}$ where the Monin–Obukhov length $\hat{L} = -\widehat{u_*^3}/(\beta\kappa\widehat{Q_*})$), von Kármán constant $\kappa = 0.4$, gravity $g = 9.81$ m s^{-2}, and reference temperature $\theta_o = 290$ K. The convective velocity scale $\widehat{w_*^3} = \beta\widehat{Q_*}\widehat{z_i}$ (Deardorff 1970). For comparison, statistics from S20 with across-front winds are listed in Table 2.

4. Results with alongfront winds

a. Far-field wind and temperature fields

The Fourier-fringe technique provides good control of the inflow turbulence in the H domain generating flow fields and coherent structures comparable to a homogeneous weakly convective marine boundary layer at the inflow boundary. To demonstrate the adequacy of the technique, we compare statistics in the far field of the H domain, at its right boundary $27.2 < x < 30.3$ km well away from the location of the jump in SST, with results from the P domain in S20 driven by across-front geostrophic winds. Low-order moments, means, variances, and vertical fluxes are shown in Figs. 2 and 3. The temperature and momentum fluxes $\langle \widehat{w'\theta'}, \widehat{u'w'}, \widehat{v'w'} \rangle_{\rm tot}$ are total values, i.e., the sum of resolved and SGS contributions. The velocity variances $\langle \widehat{u'^2}, \widehat{v'^2}, \widehat{w'^2} \rangle$ are computed from resolved fields. Additional simulations with larger domains and different fringe constants A did not appreciably change the results with alongfront winds. Results from S20 are shown with open circles with the temperature, wind components, and momentum fluxes marked by a subscript "acr".

The comparison highlights important effects. First, the vertical structure of the mean wind and temperature profiles as well as the vertical flux profiles are in rotation symmetry for the alongfront and across-front wind simulations. The former are run longer in time to obtain stable statistics and hence the boundary layer is modestly deeper and also warmer in the interior with alongfront winds, compare the right panels of Figs. 2 and 3. Consistent with Ekman dynamics alongfront geostrophic winds $V_g = 10$ m s^{-1} induce a sign change in the wind

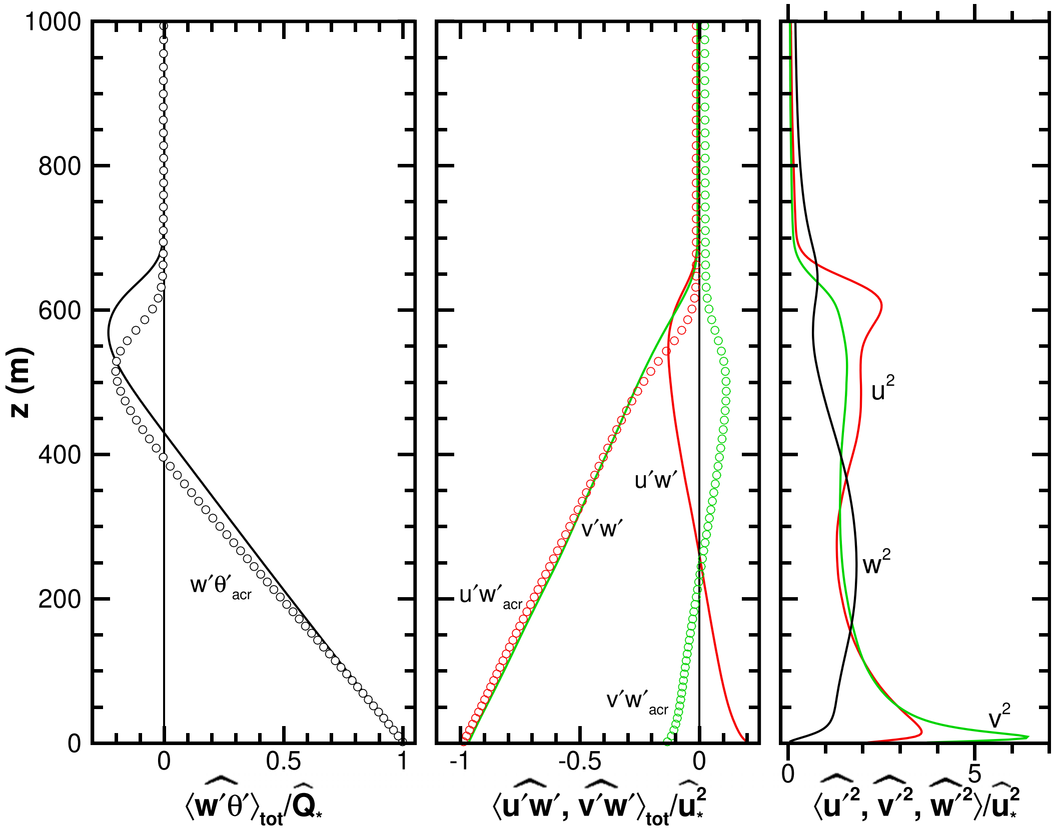

FIG. 3. Turbulence statistics in the far field with alongfront geostrophic winds. (left) Total (resolved plus SGS) temperature flux $\langle\widehat{w'\theta'}\rangle_{\rm tot}$ normalized by the surface flux $\widehat{Q}_*$, (center) total momentum fluxes $\langle\widehat{u'w'},\ \widehat{v'w'}\rangle_{\rm tot}$ normalized by $\widehat{u}_*^2$, and (right) resolved variances $\langle\widehat{u'^2},\ \widehat{v'^2},\ \widehat{w'^2}\rangle$ normalized by $\widehat{u}_*^2$. For comparison, turbulence statistics with across-front geostrophic winds from S20 are indicated by open circles; these momentum fluxes $\langle\widehat{u'w'},\widehat{v'w'}\rangle_{\rm acr}$ are indicated by red and green colors, respectively. For clarity, velocity variances from S20 are not shown in the right panel.

component $\langle\hat{u}\rangle < 0$ and near surface momentum flux $\langle\widehat{u'w'}\rangle > 0$ compared to the simulation with across-front winds $U_g = 10\,{\rm m\,s^{-1}}$. As expected, the velocity components show a 90° rotation symmetry $\langle -\hat{u},\ \hat{v}\rangle \approx \langle \hat{v},\ \hat{u}\rangle_{\rm acr}$. Also the momentum and temperature flux profiles are linear in the boundary layer interior for all the simulations indicating a quasi-steady balance. Overall, the turbulent inflow at the far right boundary of the H domain is in good agreement with the turbulent inflow in S20 when the orientation of the geostrophic winds is taken into account.

However, a key feature of the simulation with alongfront winds is the magnitude of the wind component u that blows across the SST front at $x = x_b$. With (across-front, alongfront) winds $\hat{u}$ is (parallel, perpendicular) to the imposed geostrophic wind. The ratio $-\langle\hat{u}\rangle/V_g \approx 0.17$ with alongfront winds while the same ratio with across-front winds $\langle\hat{u}\rangle_{\rm acr}/U_g \approx 0.85$. This nearly factor of 5 reduction in the wind component blowing across (perpendicular to) the SST isotherms leads to enhanced secondary circulations and modifies the statistics with alongfront winds. Also, the ratio $|\langle\hat{u}\rangle|/w_* \approx (3, 14)$ for the (alongfront, across-front) cases, respectively. Based on this metric the alongfront wind case is highly convective while the across-front wind case is moderately convective (Willis and Deardorff 1976) even though both cases have the same $-\hat{z}_i/\hat{L}$. In the narrative, we refer to u as the "ageostrophic" wind component in discussing alongfront winds.

b. Velocity patterns

The homogeneous MABL at stability $-\hat{z}_i/\hat{L} = 3.74$ is populated by coherent structures, namely, large-scale shear-convective rolls that fill the depth of the boundary layer (e.g., Moeng and Sullivan 1994; Chen et al. 2001; Sullivan et al. 2014; Patton et al. 2016; Sullivan et al. 2020). The structures are spatially coherent, temporally long-lived, and energetic. A difference between the simulations in S20 and the present study is the spatial orientation of the coherent structures. With (across-front, alongfront) geostrophic winds the axis of the rolls is primarily aligned with the (x, y) directions, respectively.

The shear-convective rolls are readily identified in flow visualization of the velocity and temperature fields in 2D cutting planes or in 3D volumes. For example, with across-front winds vertical velocity viewed in x–y planes at varying z shows coherent alternating in y updraft and downdraft lines, the lines are primarily aligned with the zonal velocity, i.e., the x axis.

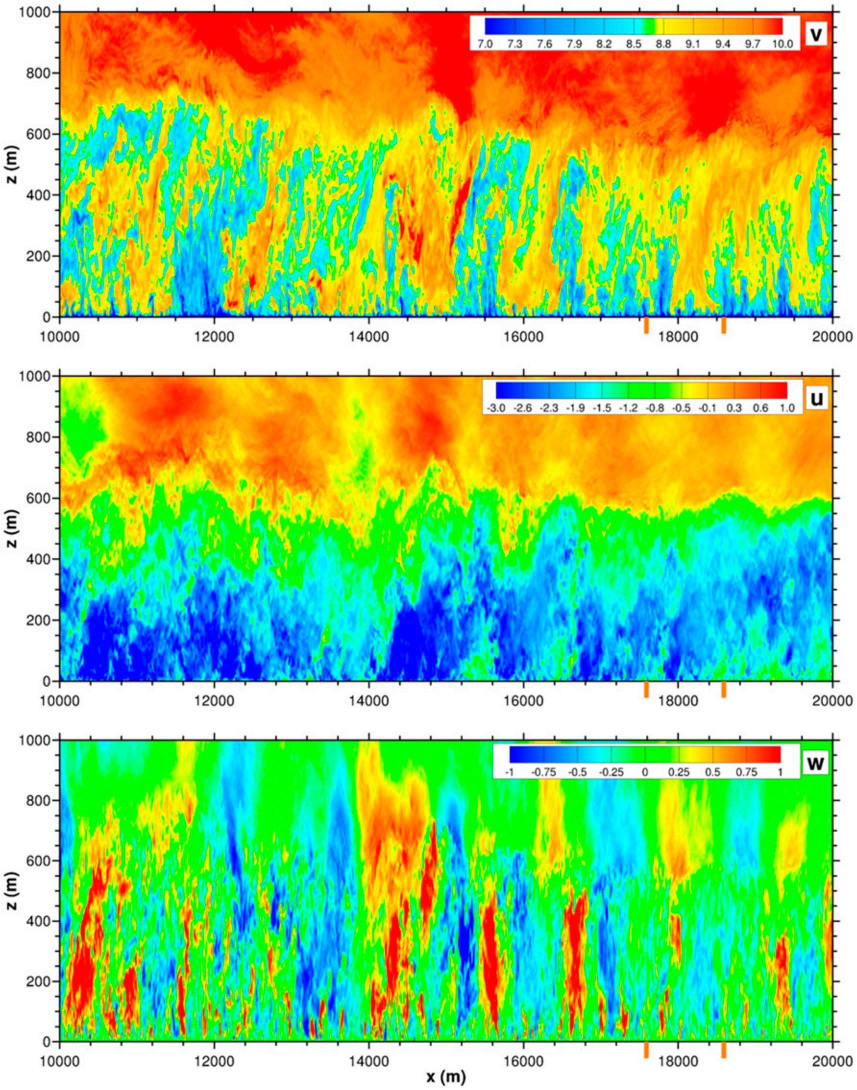

FIG. 4. Instantaneous velocity (v, u, w) in an x–z plane spanning the change in SST for a warm front. The orange vertical bars along the x axis mark the start and end of the SST jump. The color bar is in units of m s^{-1}.

Here with alongfront winds rolls are also present in the far field but are rotated approximately 90° from the x axis aligning with the wind V_g. We examine the velocity fields (v, u, w) in a 2D x–z plane perpendicular to the alongfront geostrophic wind at $y = 0.84$ km. Zooming on the interval $x = [8–20]$ km left of the SST change illustrates the impact of heterogeneous SST on the instantaneous wind patterns, see Figs. 4 and 5 for (warm front, cold front) cases, respectively. Inspection of the v patterns from case Nu1 with $\Delta\theta > 0$ shows $\langle U \rangle \approx 10\,\mathrm{m\,s^{-1}}$ at $(x, z) = (20\,\mathrm{km}, 550\,\mathrm{m})$ right of the SST and at $(x, z) = (10\,\mathrm{km}, 880\,\mathrm{m})$ left of the SST change. The hummocks and valleys in v are well correlated with the downdraft and updraft patterns in w, compare the upper and lower panels of Fig. 4. However, the most intriguing field is the spatial variability in the ageostrophic wind u blowing across the SST isotherms. Focusing on the region $10 < x < 16$ km and comparing the results with the far-field wind profile in Fig. 2 shows $u > \hat{u}$ near the top of the boundary layer while $u < \hat{u}$ in the surface layer; recall $\hat{u}$ is well mixed vertically. Thus the instantaneous flow visualization hints at a strong vertical shear layer $\partial_z u > 0$ in the middle of the boundary layer left of the SST change. Cutting planes taken at other y and t locations show similar results. A comparison with the cold front case in Fig. 5 is noteworthy. The collapse of the hummocks and valleys in v and of the updrafts and downdrafts in w illustrate the transition of the unstable boundary layer toward a stable regime left of the SST change. Now u displays an opposite pattern compared to the warm front case. In the upper middle of the MABL, between $200 < z < 400$ m $u < \hat{u}$ while near the surface $u > \hat{u}$. Thus flow visualization suggests a vigorous shear layer in the interior of the collapsing boundary layer but now $\partial_z u < 0$. Although masked by the energetic turbulence, organized secondary circulations are present in the

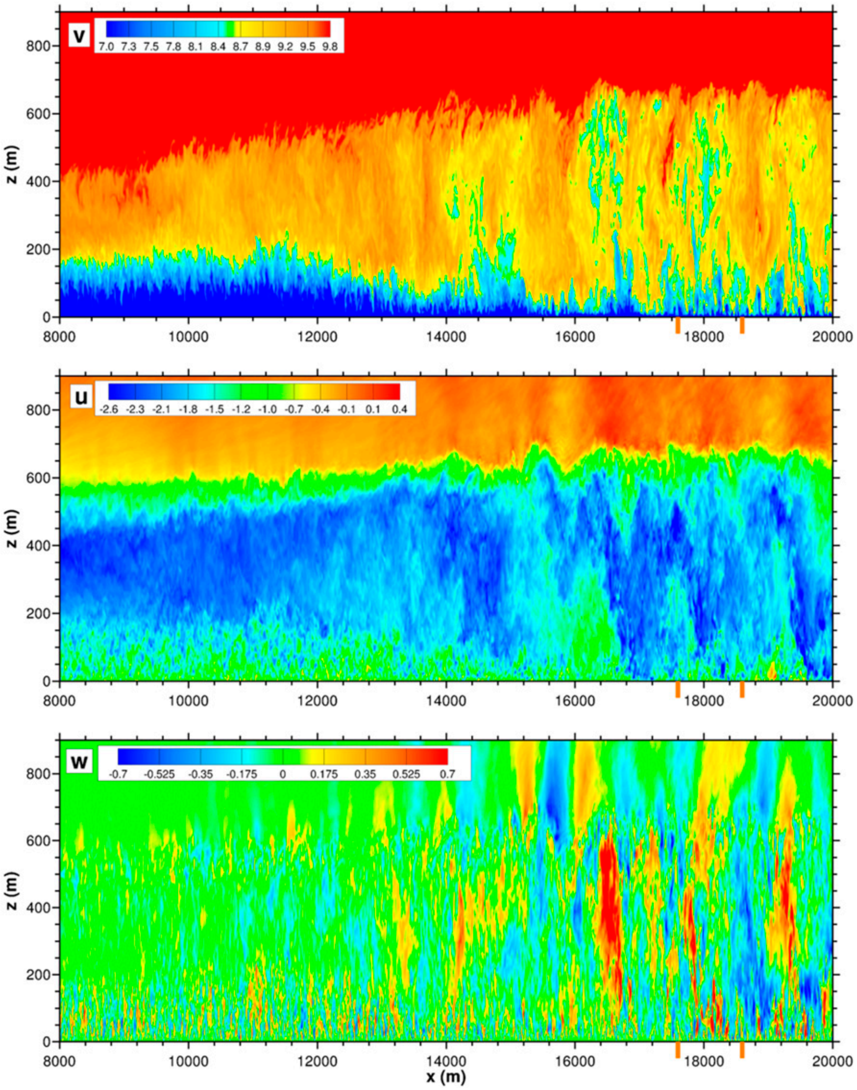

FIG. 5. Instantaneous velocity (v, u, w) in an x–z plane spanning the change in SST for a cold front. The orange vertical bars along the x axis mark the start and end of the SST jump. The color bar is in units of m s^{-1}.

instantaneous velocity and temperature fields. The secondary circulations, induced by heterogeneous SST, impact MABL mixing and surface fluxes as discussed below.

c. Surface-layer statistics

The orientation and magnitude of the geostrophic winds relative to the direction of the SST isotherms induces important changes in the surface fluxes which is illustrated by comparing results from alongfront winds with their counterparts from across-front winds. Results for the surface wind stress vector $\langle \tau_x, \tau_y \rangle$ and temperature flux $\langle Q_* \rangle$ for warm and cold SST fronts with alongfront winds are provided in Fig. 6. For reference the SST variation $\delta\theta_s(x) = \theta_s(x) - \theta_o$ is provided in the bottom panel of Fig. 6. The wind stress components are shown on opposite vertical axes with different ranges in the upper panel of Fig. 6, and the surface fluxes of momentum and temperature are normalized by their respective values in the far field, viz., $(\widehat{u_*^2}, \widehat{Q_*})$. Recall with positive alongfront geostrophic winds the ageostrophic surface wind $u < 0$ and hence $\tau_x > 0$.

First notice Q_* closely tracks the spatial variation of SST, especially in the warm front case. Recall SST appears as a boundary condition in the bulk formula for temperature flux at the first model level in the LES which then closely couples Q_* and θ_s as discussed in S20. The response of the surface momentum flux is spatially delayed compared to the change in SST more so in the cold front case. It is especially noteworthy that the ageostrophic component of the wind stress $\tau_x/\widehat{u_*^2}$ (increases, decreases) by a factor of 2 or more left of the SST change for the (warm front, cold front) cases, respectively. As discussed later in section 4d, the change in $\tau_x/\widehat{u_*^2}$ is a consequence of SST induced secondary circulations left of x_b. In the

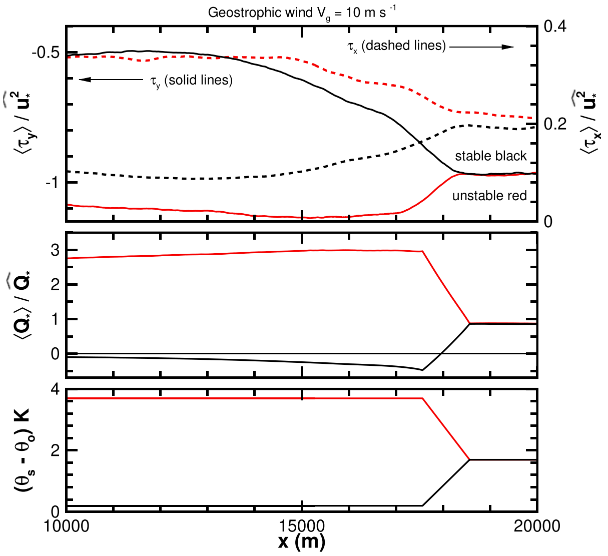

FIG. 6. (top),(middle) Spatial variation of surface-layer variables $\langle \tau_x, \tau_y, Q^* \rangle$ for warm (unstable) and cold (stable) SST fronts with alongfront geostrophic winds $V_g = 10\,{\rm m\,s^{-1}}$. (bottom) The x variation of SST $\delta\theta_s(x) = \theta_s(x) - \theta_o$. The surface momentum and temperature fluxes are normalized by $(\widehat{u_*^2}, \widehat{Q*})$, respectively. In the top panel, the (dashed, solid) lines denote (τ_x, τ_y), and the (red, black) colors denote (warm, cold) changes in SST.

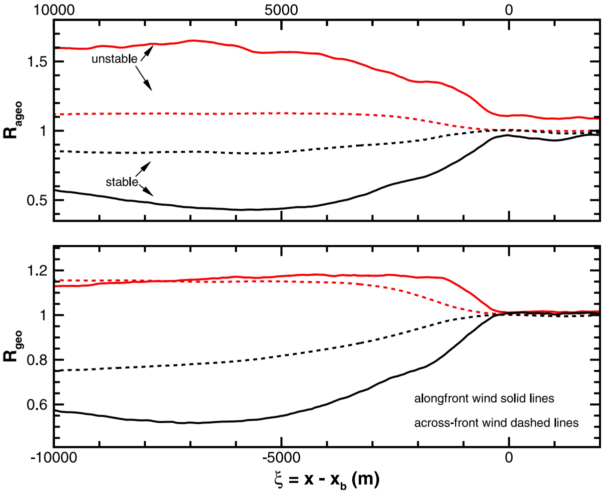

FIG. 7. Spatial variation of the surface stress ratios $(R_{\rm ageo}, R_{\rm geo})$ perpendicular and parallel to the imposed geostrophic wind; see Eq. (6). The (solid, dotted) lines are (alongfront, across-front) winds with $(V_g, U_g) = 10\,{\rm m\,s^{-1}}$, respectively. Simulations (Nu1, Ns1) with (unstable, stable) changes in SST are indicated by (red, black) lines, respectively. The ratios are normalized by their respective values in the far field. To readily illustrate the comparisons, the variations are shown relative to the breakpoint x_b where the SST first starts to change, i.e., $\xi = x - x_b$. Note that the abscissa in the simulations with across-front geostrophic winds from S20 is reversed increasing from right to left.

cold front simulation, the ageostrophic wind $u \to 0$ left of x_b which is nearly sufficient to induce a sign change in τ_x compared to its far-field value. The variation of the average near surface winds (u, w) is discussed in section 4d.

To illustrate the impact of alongfront versus across-front winds on the surface stress we introduce (geostrophic, ageostrophic) surface stress ratios $(R_{\rm geo}, R_{\rm ageo})$ aligned with the x and y directions:

$$(R_{\rm geo}, R_{\rm ageo}) = (\tau_y/\widehat{\tau}_y, \tau_x/\widehat{\tau}_x): V_g = 10\,{\rm m\,s^{-1}}, \qquad (6a)$$

$$(R_{\rm geo}, R_{\rm ageo}) = (\tau_x/\widehat{\tau}_x, \tau_y/\widehat{\tau}_y): U_g = 10\,{\rm m\,s^{-1}}, \qquad (6b)$$

where $(\widehat{\tau}_x, \widehat{\tau}_y)$ are values computed in the far field. This normalization allows a fair comparison between cases with alongfront and across-front winds. The x variation of the ratios in (6a) are shown in Fig. 7 using a common horizontal distance measured relative to the location where the SST change starts $\xi = x - x_b$: $x_b = (18.6, 2.7)$ km for (alongfront, across-front) winds, respectively. The important message in Fig. 7 is that for a fixed geostrophic wind magnitude the momentum fluxes are sensitive to SST changes depending on the magnitude and direction of the surface winds. The percentage change in the wind stress components compared to their far-field values is greater with alongfront winds, especially in the case of a transition to a stable boundary layer regime. This is a consequence of persistent secondary circulations (SC) induced with alongfront winds.

The secondary circulations also impact the divergence and curl of the surface wind stress. Because of the homogeneity in the y direction, $\langle \nabla \cdot \boldsymbol{\tau} \rangle = \partial_x \langle \tau_x \rangle$ and $\langle \nabla \times \boldsymbol{\tau} \rangle = \partial_x \langle \tau_y \rangle$. With alongfront winds the curl of wind stress is larger (in magnitude) than the divergence of the wind stress (not shown); this is pronounced in the cold front case, i.e., when the flow transitions from unstable to stable surface-layer turbulence. Previously, S20 found the divergence of wind stress is larger than the curl of wind stress with across-front winds. Also the curl of the wind stress is larger with the transition from warm-to-cold as opposed to the transition from warm-to-warmer. This shows changes in wind stress and SST are correlated but dependent on surface-wind–SST orientation and stability, at least for the small-scale changes in SST considered here.

d. *Secondary circulations (SC)*

In the MABL with heterogeneous SST turbulence, coherent structures and SC each of varying amplitude and scale coexist; the origin of the SC is discussed below. To extract the SC from the turbulent fields, for example in Fig. 4, we use unconditional space–time averaging, i.e., no attempt is made to statistically identify the turbulence structures separately. The velocity perturbations of the SC are simply defined as average deviations from the far field $(u_p, v_p, w_p) = (\langle u - \hat{u} \rangle, \langle v - \hat{v} \rangle, \langle w \rangle)$ where the space–time averaging operator $\langle\,\rangle$ is defined in section 3c; note that in the far field the boundary layer is nearly horizontally homogeneous and then $\langle \hat{w} \rangle = 0$. Two-dimensional x–z fields of (u_p, w_p) for (warm, cold) front simulations are shown in the visualizations presented in Figs. 8 and 9, respectively. The streamfunction ψ_p computed from $\int u_p\, dz$ is shown in Figs. 10

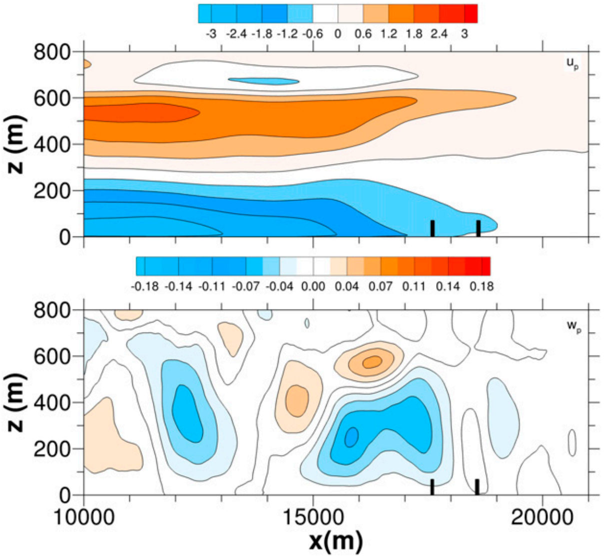

FIG. 8. Secondary circulation velocity fields (top) u_p and (bottom) w_p for a warm front. The perturbation fields are normalized by $\widehat{u_*}$. The black vertical bars along the x axis mark the start and end of the SST front. At $x = (17.56, 18.56)$ km, the SST $\theta_s = (\theta_c + 2\,\mathrm{K}, \theta_c)$, respectively.

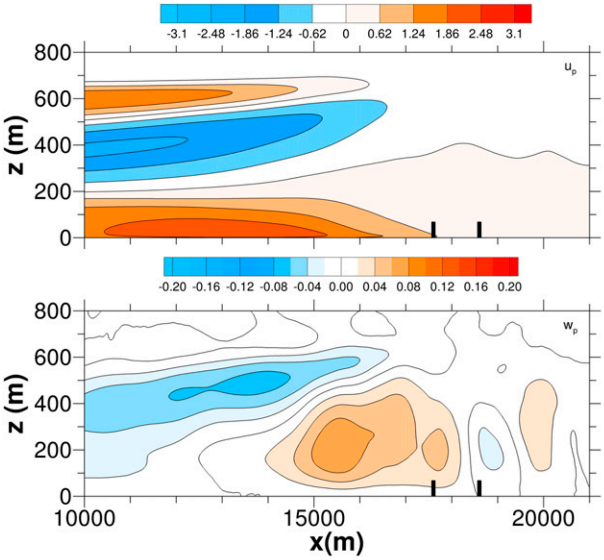

FIG. 9. Secondary circulation velocity fields (top) u_p and (bottom) w_p for a cold front. The black vertical bars along the x axis mark the start and end of the SST front. At $x = (17.56, 18.56)$ km, the SST $\theta_s = (\theta_c - 1.5\,\mathrm{K}, \theta_c)$, respectively.

and 11. The velocity perturbations and streamfunction are normalized by $1/\widehat{u_*}$ and $\widehat{z}_i/\widehat{u_*}$, respectively.

Inspection of the results readily shows persistent organized patterns in (u_p, w_p) in both warm and cold fronts despite the high levels of turbulence in Figs. 4 and 5. It is insightful to compare the amplitudes of the SC with each other and also with the mean ageostrophic wind and turbulence in Figs. 2 and 3. In the warm front case, the peak amplitudes $w_p/u_p \sim 0.03$ and the vertical turbulence in the middle of the boundary layer $w_p/\sqrt{\langle w'^2\rangle} \sim 0.05$. The maximum downdraft $w_p \sim \mathcal{O}(2\ \mathrm{cm\ s^{-1}})$ is noteworthy; it is nearly a factor of 10 larger than typical entrainment rates and maximum downdraft found at the top of the boundary layer with across-front winds, see Fig. 12 in S20. The peak magnitude of the horizontal component $u_p \sim 0.44\langle\hat{u}\rangle$ and compared to the horizontal turbulence near the surface $u_p \geq \sqrt{\langle u'^2\rangle}$. Similar peak amplitudes (u_p, w_p) are found in the cold front case but with opposite signs. The variation of the surface stress τ_x in Fig. 6 is a direct consequence of the near surface large amplitude and sign of u_p; notice $u_p > 0$ for the cold front case. Importantly, notice the perturbations (u_p, w_p) exhibit spatial organization at kilometer scales horizontally with a vertical scale $\sim z_i$, which is especially apparent in u_p.

In the streamfunction plots (Figs. 10 and 11) the smoothed black curve annotated with an arrowhead is a subjective drawing indicating the direction of the SC rotation. Note the SC patterns are shifted slightly left of the location of the SST change presumably by the the weak ageostrophic wind and also more importantly by the horizontal pressure gradients. Based on the streamfunction we can identify two-classes of SC in the simulations. In the warm front case the SC is open at the left end, i.e., the horizontal extent of the rotation fills the interval $10 < x < 18$ km. The clockwise rotation features a downwelling branch near $x \sim 17$ km with nearly uniform negative and positive u_p regions at the bottom and top of the boundary layer. In this simulation the horizontal to vertical aspect ratio of the elliptical pattern >10. This open pattern of SC features stronger rotation and is located much closer to the change in SST compared to the simulation with strong across-front winds in S20.

In the cold front case the SC patterns are sign reversed but now feature a closed counterclockwise rotation, i.e., the rotation is confined within the LES domain, $10 < x < 18$ km; upwelling and downwelling branches at the ends close the circulation. The SC show (positive, negative) perturbations in u_p at the (top, surface) of the boundary layer and (updrafts, downdrafts) at the left and right ends close the rotation. A rough estimate indicates the horizontal–vertical aspect ratio of the SC exceeds 10. The persistence of the SC is responsible for the variations in the instantaneous fields observed in Figs. 4 and 5. In their horizontally periodic simulations, Wenegrat and Arthur (2018) also find velocity and temperature patterns at the 10-m height shifted horizontally from the location of the SST gradients.

How are the secondary circulations in Figs. 8 and 9 generated and maintained and how do they vary depending on the direction of the geostrophic winds, i.e., alongfront or across-front? To investigate the dynamics we introduce the average momentum balances derived from the LES equations. Adopting the decomposition (4) and applying the spatial averaging rules outlined in section 3c to (1a) and (1b) results in the (x, y) momentum balances in H:

$$\begin{aligned}\partial_t\langle u\rangle &= f(\langle v\rangle - V_g) - \langle\partial_x p\rangle - \langle u\rangle\partial_x\langle u\rangle - \langle w\rangle\partial_z\langle u\rangle \\ &\quad - \partial_z\langle u'w' + \tau_{uw}\rangle - \partial_x\langle u'u' + \tau_{uu}\rangle,\end{aligned} \tag{7a}$$

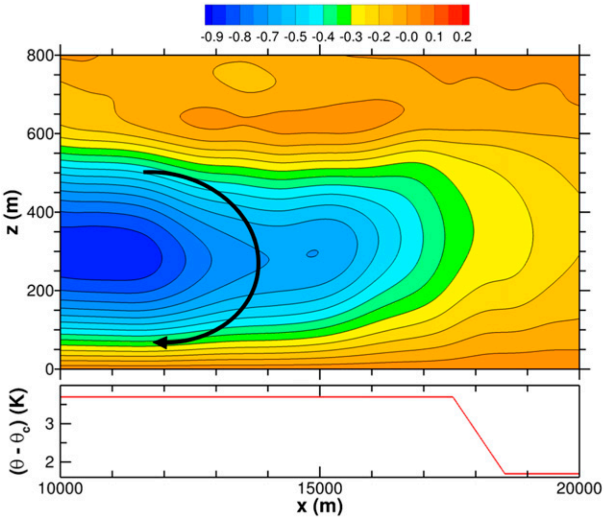

FIG. 10. (top) Streamfunction ψ_p computed from the secondary circulation wind u_p normalized by $\widehat{z_i}/\widehat{u_*}$ for a warm front. The shaded contours are evenly spaced. The black stream trace highlights the average direction of the secondary circulation. (bottom) The variation of the SST $\langle \theta - \theta_c \rangle$ with x. The far-field ageostrophic wind $\langle u \rangle$ is from right to left.

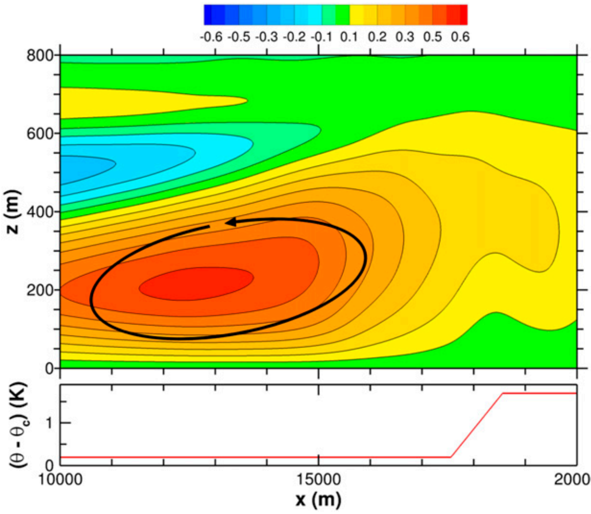

FIG. 11. (top) Streamfunction ψ_p computed from the secondary circulation wind u_p normalized by $\widehat{z_i}/\widehat{u_*}$ for a cold front. The black stream trace highlights the average direction of the secondary circulation. (bottom) The variation of the SST $\langle \theta - \theta_c \rangle$ with x. The far-field ageostrophic wind $\langle u \rangle$ is from right to left.

$$\partial_t \langle v \rangle = f(U_g - \langle u \rangle) - \langle u \rangle \partial_x \langle v \rangle - \langle w \rangle \partial_z \langle v \rangle - \partial_z \langle v'w' + \tau_{vw} \rangle - \partial_x \langle u'v' + \tau_{uv} \rangle . \tag{7b}$$

At the same time, the average homogeneous momentum balances in the far field are as follows:

$$\partial_t \langle \hat{u} \rangle = f(\langle \hat{v} \rangle - V_g) - \partial_z \widehat{\langle u'w' + \tau_{uw} \rangle} , \tag{8a}$$

$$\partial_t \langle \hat{v} \rangle = f(U_g - \langle \hat{u} \rangle) - \partial_z \widehat{\langle v'w' + \tau_{vw} \rangle} . \tag{8b}$$

Next, subtract (8) from (7) which results in unsteady (x, y) momentum balances for the secondary circulations $\langle u_p, v_p \rangle = \langle u, v \rangle - \langle \hat{u}, \hat{v} \rangle$:

$$\partial_t \langle u_p \rangle = \underbrace{f \langle v_p \rangle}_{C_{\text{or}}} - \underbrace{\langle \partial_x p \rangle}_{P_x} - \underbrace{\langle u \rangle \partial_x \langle u_p \rangle}_{H_{\text{adv}}} - \underbrace{\langle w \rangle \partial_z \langle u \rangle}_{V_{\text{adv}}} - \underbrace{\partial_x \langle u'u' + \tau_{uu} \rangle}_{H_{\text{div}}} - \underbrace{\partial_z \langle u'w' + \tau_{uw} \rangle + \partial_z \widehat{\langle u'w' + \tau_{uw} \rangle}}_{V_{\text{div}}} , \tag{9a}$$

$$\partial_t \langle v_p \rangle = -f \langle u_p \rangle - \langle u \rangle \partial_x \langle v_p \rangle - \langle w \rangle \partial_z \langle v \rangle - \partial_x \langle u'v' + \tau_{uv} \rangle - \partial_z \langle v'w' + \tau_{vw} \rangle + \partial_z \widehat{\langle v'w' + \tau_{vw} \rangle} . \tag{9b}$$

Equations (9a) and (9b) are interesting. First, they are coupled in their Coriolis, advective, and divergence of turbulence flux terms. And second the circulations are driven by spatially varying horizontal pressure gradients $\langle \partial_x p \rangle$ and by vertical wind gradients, i.e., $\partial_z \langle u, v \rangle = \partial_z \langle u_p, v_p \rangle + \partial_z \langle \hat{u}, \hat{v} \rangle$. Under the assumptions of steady flow, weak horizontal gradients, and negligible advection, then (9a) and (9b) can be interpreted as a form of so-called turbulent thermal wind (TTW) (Gula et al. 2014; McWilliams 2018; Sullivan and McWilliams 2019). McWilliams et al. (2015) used TTW and a single column boundary layer parameterization to diagnose how turbulent fluxes in the upper ocean can drive secondary circulations that force ocean frontogenesis (McWilliams 2020). TTW was extended to include nonlinear effects by McWilliams (2018).

Dominant terms on the right-hand side of the perturbation x momentum equation, Eq. (9a), are evaluated for alongwind and across-wind geostrophic winds for varying x. Typical results near the surface and boundary layer top are compared in Figs. 12 and 13, respectively. The vertical range in the figures is the same and terms are normalized by $-\widehat{u_*^2}/\widehat{z_i}$. Terms with underbraces in (9a) correspond to the labeling in the two figures. Inspection of Fig. 12 shows that large horizontal pressure gradients $\langle \partial_x p \rangle$ play a dominate role in the alongfront wind simulation, i.e., when the ageostrophic wind perpendicular to the SST isotherms is weak. Recall $-\langle \hat{u} \rangle / \langle \hat{u} \rangle_{\text{acr}} \sim 0.2$ in Fig. 2. The large positive pressure gradient near the surface drives u_p to the left of the SST jump, while the large negative pressure gradient near the boundary layer top drives u_p to the right of the SST jump. The vertical divergence of turbulence flux opposes the pressure gradient for $x < 16$ km. Horizontal advection is important at all levels while near the boundary layer top vertical advection from the SC $\langle w \rangle \partial_z \langle u \rangle$ also contributes to the momentum budget. The perturbation x momentum budget with across-front winds in Fig. 13 features a strikingly different balance of terms. Now the horizontal pressure gradient by comparison is quite small and remains finite at large x away from the SST change. The pressure gradient slightly increases the surface-layer winds but slows the winds near the boundary layer top at all x. Horizontal advection is balanced by vertical flux divergence.

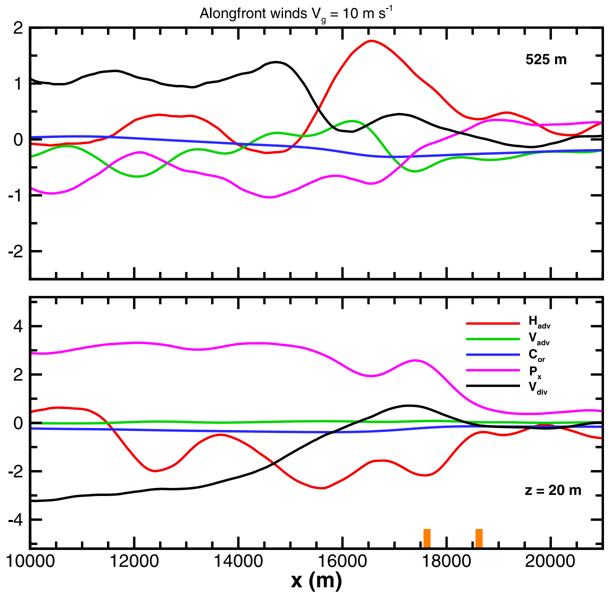

FIG. 12. Terms in the perturbation x momentum budget equation, Eq. (9a), at z = (bottom) 20 and (top) 525 m with alongfront winds above a warm front. The boundary layer ageostrophic wind u is from right to left. The start and end of the change in SST is indicated by the orange vertical bars along the x axis. The line labeling corresponds to the terms with underbraces in Eq. (9a).

With alongfront geostrophic winds the ageostrophic wind component is weak and then organized horizontal baroclinic pressure gradients spring to life. The spatial structure of the horizontal pressure gradients for (warm, cold) front simulations are compared in Fig. 14. The gradients which are of opposite sign at the bottom and top of the boundary layer drive the secondary circulations left of the change in SST. The pressure field in the LES is 3D, but when averaged in the alongfront y direction, the average pressure field is the solution of a 2D elliptic Poisson equation (e.g., Moeng and Wyngaard 1986; Pope 2000):

$$\left(\frac{\partial^2}{\partial x^2}+\frac{\partial^2}{\partial z^2}\right)\overline{p}=\frac{\partial}{\partial x}\left(-\overline{u\frac{\partial u}{\partial x}}-\overline{w\frac{\partial u}{\partial z}}+\cdots\right)+\frac{\partial}{\partial z}\left(-\overline{u\frac{\partial w}{\partial x}}-\overline{w\frac{\partial w}{\partial z}}+\beta\overline{\theta}+\cdots\right), \qquad (10)$$

where the source term includes horizontal and vertical advection, buoyancy, and the ellipses denote all the other terms on the right-hand side of (1a); as written, the advection terms in (10) contain mean, SC, and turbulence contributions. Apparently when horizontal advection $\overline{u\partial_x u}$ is weak the vertical gradients of buoyancy $\beta\partial_z\overline{\theta}$ at the bottom and top of the boundary layer contribute significantly to the pressure solution. The generation of perturbation winds and SC in the atmospheric boundary layer with heterogeneous SST is then a complex dynamical balance that depends on horizontal pressure gradients, the magnitude and direction of horizontal advection, and turbulence flux divergence. For these simulations, apparently (9a) does not reduce to a simple linear momentum balance as assumed in TTW because of nonlinear mean horizontal advection.

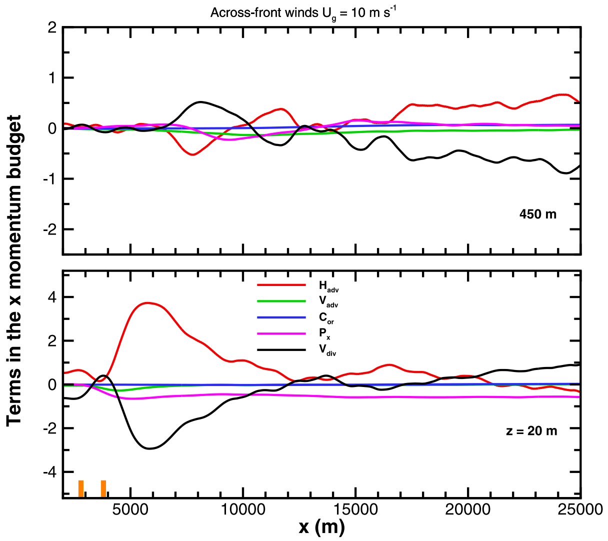

FIG. 13. Terms in the perturbation x momentum budget equation, Eq. (9a), at z = (bottom) 20 and (top) 450 m for simulation Eu2 with across-front winds above a warm front from S20. The u component of the boundary layer wind is from left to right. The start and end of the change in SST is indicated by the orange vertical bars along the x axis.

e. *Winds, temperature, and vertical fluxes*

Analysis and flow visualization of the LES database with alongfront winds shows SC impact the mean wind and temperature but also the important details of the turbulence momentum and temperature fluxes and velocity variances. SC modulate the vertical transport between the bottom and top of the boundary layer over an extended horizontal region left of the SST change; their impact on mixing, however, depends on the thermal stratification. Similar to S20 the variation of the turbulence statistics is not spatially monotonic in the interval left of the SST change, i.e., in the interval $10 < x < 18$ km. To demonstrate these ideas we present 2D contours of the total vertical momentum flux $\langle u'w'\rangle$ and vertical profiles of $\langle \theta,\ u,\ u',\ w'\theta,\ U,\ U'w'\rangle$ at particular x locations in Fig. 15. The far-field boundary layer is weakly unstable with the inflow wind and temperature profiles well mixed as shown in Fig. 2. In simulation Nu1, heterogeneous SST disrupts the shape of the mean profiles. In the region $10 < x < 18$ km the temperature profile retains its well-mixed shape, but the ageostrophic wind shows persistent vertical shear $\partial_z\langle u\rangle$ despite the unstable thermal forcing, see the top row, middle panel of Fig. 15. The clockwise rotation of the SC increases the surface winds and decreases the winds at the top of the boundary layer. The vertical shear, which reaches a maximum in the middle of the boundary layer $z \sim 300$ m, generates high levels of turbulent momentum flux $-\langle u'w'\rangle$. The flux magnitude is large $-\langle u'w'\rangle \sim 0.85\widehat{u_*^2}$ and is opposite in sign and 3 times larger than the surface stress τ_x shown in Fig. 6. The horizontal extent of the region with enhanced momentum flux is broad x = [10–

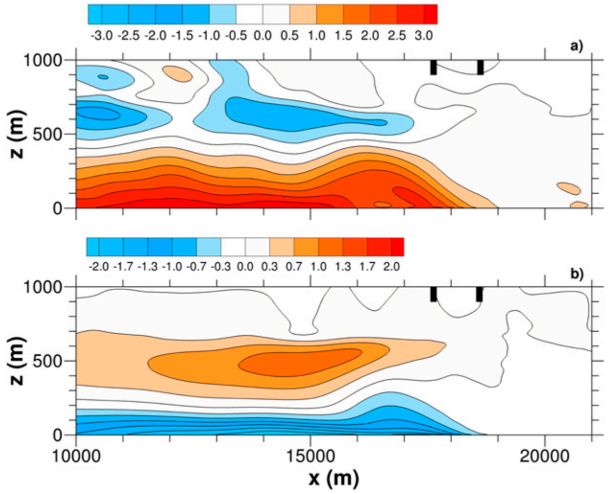

FIG. 14. Contours of the horizontal pressure gradient $\partial_x\langle p\rangle$ normalized by $-\widehat{z_i/u_*^2}$ with alongfront winds. Over a horizontal distance $\ell = 1$ km, the SST change is (a) $\Delta\theta = 2$ K, warm front case, and (b) $\Delta\theta = -1.5$ K, cold front case. In both cases, the ageostrophic wind is from right to left. The start and end of the SST jump is marked by the black vertical bars, see Fig. 1.

17] km. Because of the SC the vertical flux divergence $\partial_z\langle u'w'\rangle$ between the surface and flux maximum in the middle of the boundary layer is large.

Next, consider the cold front case where the flow is stably stratified left of the SST change; see Fig. 16. Now the SC has an opposite effect compared to Nu1 it reduces mixing and promotes stably stratified turbulence. Figure 11 shows a counterclockwise rotating SC and its magnitude is nearly sufficient to reverse the direction of the surface winds. As a result the surface stress τ_x is greatly reduced as shown in Fig. 6. The SC rotation reduces the magnitude and sign of the vertical shear $\partial_z\langle u\rangle$ in the interior of the boundary layer which in turn weakens the turbulence production. In the cold front case, in the region say $10 < x < 18$ km the SC promotes stably stratified turbulence, an opposite effect compared to the warm front case. As the SC decays, for example at $x = 10$ km in Fig. 16, the stable stratification at the surface is weaker and the boundary layer properties tend to a weakly stratified regime; this is shown by comparing the θ profiles at $x = (10, 16)$ km with the far-field θ profile; see bottom row, left panel of Fig. 16. There are also significant changes in the alongfront momentum flux $\langle v'w'\rangle$; see bottom row, right panel in Fig. 15. The latter is not linear in z and shows a collapse left of the change in SST which leads to an increase in the alongfront wind $\langle v\rangle$ over a greater depth in the boundary layer; see bottom row, middle panel of Fig. 15.

Vertical temperature flux couples the heterogeneous ocean surface with boundary layer entrainment, and ultimately with low-level cloud formation (Atkinson and Zhang 1996). The bottom-left panels of Figs. 15 and 16 show single column vertical profiles of normalized temperature flux $\langle w'\theta'\rangle/\widehat{Q}_*$ at selected x positions left of the SST change. Companion two-dimensional contours of temperature flux are depicted in Fig. 17. In Fig. 15, notice the vertical temperature flux profiles are not linear in z but slightly concave left of the change in SST. More importantly over the interval $x = [10\text{–}18]$ km the minimum entrainment flux $\langle w'\theta'\rangle_e/\widehat{Q}_* \sim -0.2$ despite a nearly factor of 3 increase in surface temperature flux; the interior of the boundary layer warms considerably as shown in the profiles of temperature, left panel in the top row of Fig. 15. In the far field $\langle\widehat{w'\theta'}\rangle/\widehat{Q}_* = -0.2$ as shown in Fig. 3. Hence the usual assumption for entrainment flux parameterization does not hold in the vicinity of a warm front with alongfront winds because of the downwelling induced by the SC. In Fig. 17 the temperature flux contours are surprisingly similar in shape to those in S20 (Figs. 19 and 20) taking into account the difference in sign of the u wind component. In the case of the warm SST front, tracing a constant contour shows a near linear increase in z with decreasing x left of the SST change. Similar to S20, the temperature flux also displays an overshoot followed by relaxation followed by a smooth slow increase with decreasing x. However because of the weak ageostrophic wind the overshoot is located much closer to the change in SST compared to the case with across-front winds by a factor of 4 which is slightly less than the ratio of $u_{\text{acr}}/|u|$, see discussion in section 4a. The entrainment flux is also lower with alongfront winds. The maximum normalized entrainment flux is ~ -0.4 at $x = 3$ km left of the SST change; at this location the normalized surface flux $\langle Q_*\rangle/\widehat{Q}_* \sim 3$, see Fig. 6. Both Figs. 16 and the lower panel of Fig. 17 show a turbulence collapse in the upper boundary layer and transition from a weakly convective unstable regime to a weakly stable regime. Broadly, the surface-wind orientation relative to the SST isotherms, is then a key factor influencing the coupling between the atmosphere and sea surface.

f. Parameter variations

The richness of possible SST states and surface-wind orientations permits numerous responses in the MABL; it is infeasible to explore all of them. In S20 and the present work we examined single-sided warm and cold SST fronts. Figure 18 illustrates the complexity of motions that can be generated in the MABL by alongfront winds in the case of warm and cold filaments. Cold filaments are important for upper-ocean mixing (e.g., Sullivan and McWilliams 2018, 2019). A warm filament is a combination of cold-warm and warm-cold fronts separated by a small finite distance. In Fig. 18 the SST jump is $\Delta\theta = (2, -2)$ K separated by a 1 km middle region; the full width of the filament $3\ell = 3$ km. Swapping the horizontal positions of the fronts in a warm filament generates a cold filament. In our configuration, the streamfunctions show the warm filament generates a pair of closed secondary circulations that are a combination of the secondary motions in Figs. 10 and 11. The strength and size of the SC are asymmetrical, left of the filament centerline $x_b = 12$ km the clockwise circulation generated by $\Delta\theta > 0$ is stronger and wider than the counterclockwise circulation centered near $x \sim 3$ km generated by $\Delta\theta < 0$. The SC combine to generate an updraft in the central middle region $x \sim 7$ km. Meanwhile the cold filament also generates SC but with opposite signs of rotation thus generating a downdraft in the middle region The response of

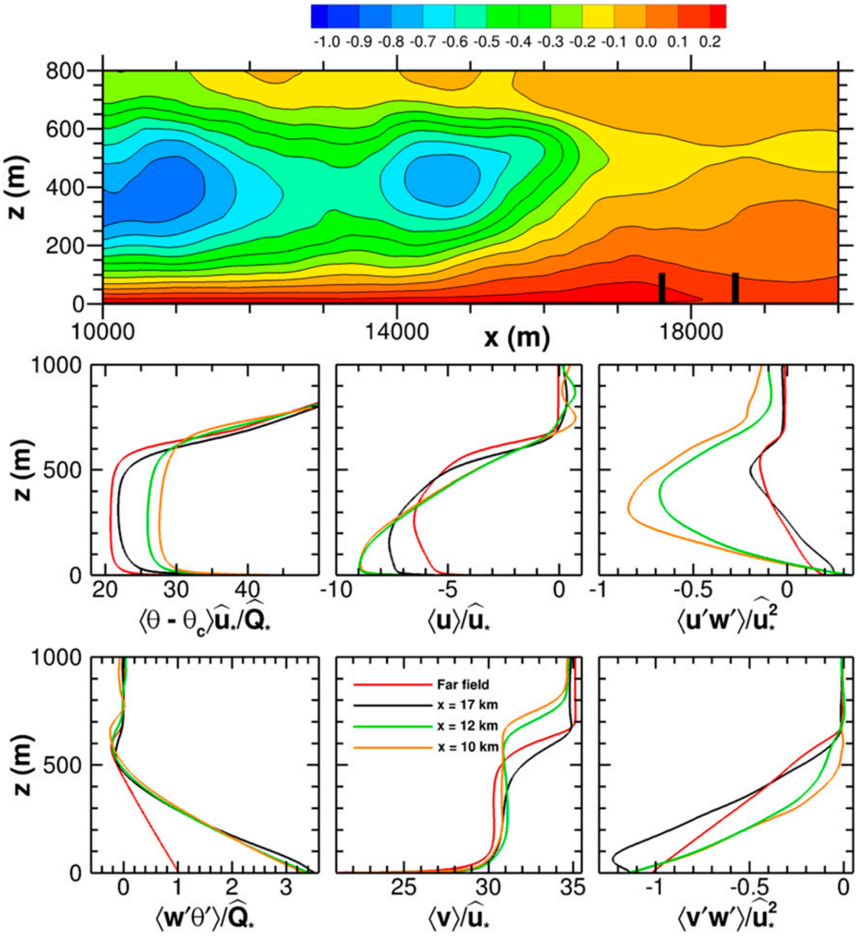

FIG. 15. Results from the simulation above a warm front. (top) Contours of total momentum flux $\langle u'w'\rangle/\widehat{u_*^2}$. The black vertical bars denote the start and end of the SST jump. Also shown are the average vertical profiles of (middle left to middle right) temperature $\langle\theta - \theta_c\rangle\widehat{u_*}/\widehat{Q_*}$, ageostrophic wind $\langle u\rangle/\widehat{u_*}$, and total momentum flux $\langle u'w'\rangle/\widehat{u_*^2}$ and (bottom left to bottom right) total temperature flux $\langle w'\theta'\rangle/\widehat{Q_*}$, alongfront wind $\langle v\rangle/\widehat{u_*}$, and total momentum flux $\langle v'w'\rangle/\widehat{u_*^2}$. Profiles are denoted at $x = 10$ (green), 12 (orange), and 17 km (black) and the red line denotes profiles in the far field.

the MABL to cold filaments is important because Gula et al. (2014) finds elongated cold (dense) filaments are pervasive in the ocean submesoscale regime compared to warm filaments, also see the synthetic aperture radar images in McWilliams et al. (2009). Our estimates of the x perturbation momentum budget also find that horizontal pressure gradients and mean advection are important similar to the results with single-sided fronts.

Figure 19 is a companion to Fig. 18 and shows the effect of filaments on the resolved (normalized) vertical temperature flux $\langle w'\theta'\rangle/\widehat{Q_*}$. In both cases, the most potent impact on the vertical flux occurs near the middle of the filaments at $x = 12$ km where the largest increase or decrease to the surface temperature flux occurs. The SC in the cold filament can also be spotted in Fig. 19 over the region $x = [6–10]$ km near the boundary layer top where the SC reduces the normalized entrainment ratio compared to the far-field value -0.2, see Fig. 3. For example, the normalized ratio ~ 0 at $(x, z) = (8, 600)$ km. This is noteworthy, cold filaments are common in the upper ocean (McWilliams et al. 2009), and can potentially impact low-level cloud formation (Atkinson and Zhang 1996). In contrast, warm filaments modestly increase the entrainment, e.g., near the center of the SC in Fig. 18 the normalized ratio ~ -0.33.

5. Summary and discussion

High-Reynolds-number large-eddy simulation (LES) is used to simulate weakly convective marine atmospheric boundary layers (MABL) forced by a combination of geostrophic winds $V_g = 10\,\mathrm{m\,s^{-1}}$ and spatially heterogeneous sea surface temperature (SST). The SST heterogeneity is time invariant and varies solely in the x direction, and the imposed one-sided SST fronts feature jumps $\Delta\theta$ between two temperature levels over a

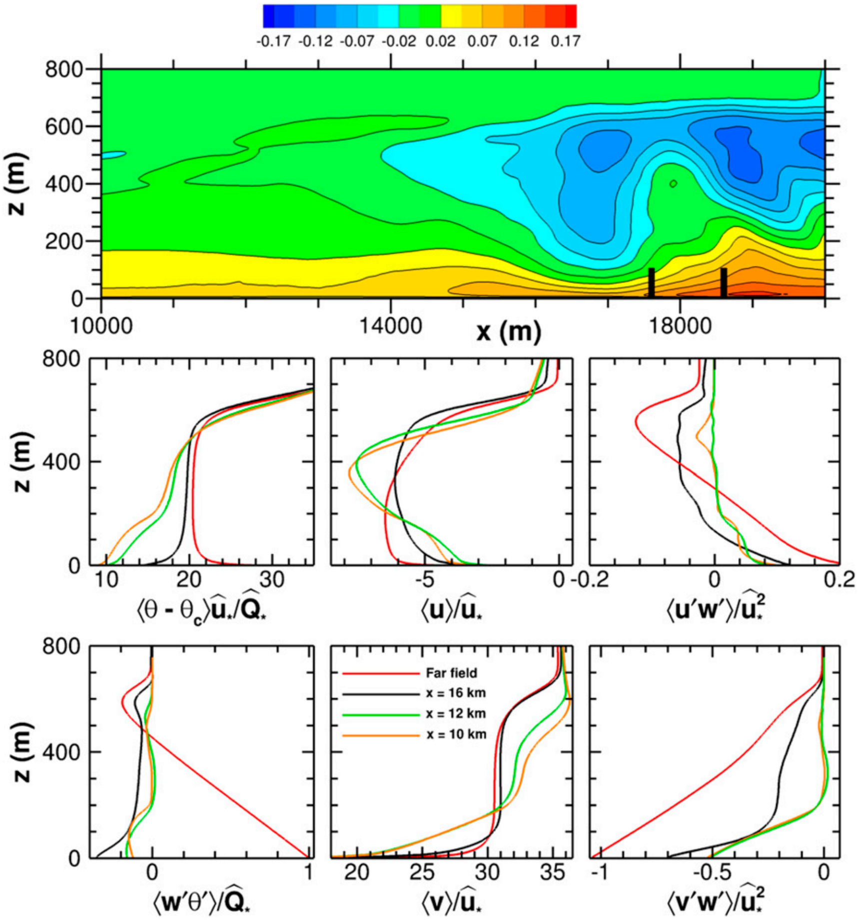

FIG. 16. Results from the simulation above a cold front. (top) Contours of total momentum flux $\langle u'w'\rangle/\widehat{u_*^2}$. The black vertical bars denote the start and end of the SST jump. Also shown are the average vertical profiles of (middle left to middle right) temperature $\langle\theta-\theta_c\rangle\widehat{u_*}/\widehat{Q_*}$, ageostrophic wind $\langle u\rangle/\widehat{u_*}$, and total momentum flux $\langle u'w'\rangle/\widehat{u_*^2}$, and (bottom left to bottom right) total temperature flux $\langle w'\theta'\rangle/\widehat{Q_*}$, alongfront wind $\langle v\rangle/\widehat{u_*}$, and total momentum flux $\langle v'w'\rangle/\widehat{u_*^2}$. Profiles are denoted at x = 10 (green), 12 (orange), and 16 km (black) and the red line denotes profiles in the far field.

finite distance $\ell = 1$ km characteristic of an ocean mesoscale or submesoscale regime. Positive warm front and negative cold front temperature jumps $\Delta\theta = (2, -1.5)$ K are considered. The geostrophic wind is oriented parallel to the imposed SST isotherms, i.e., a regime with "alongfront winds." In the x direction turbulent inflow–outflow boundary conditions are prescribed using a numerical "Fourier-fringe" technique described in S20. Grid meshes of 2.2×10^9 points with fine resolution (horizontal, vertical) spacing $(\delta x = \delta y, \delta z) = (4.4, 2)$ m are used. Previously, S20 considered similar MABLs forced by geostrophic winds oriented perpendicular to the imposed SST isotherms, i.e., a regime with "across-front" winds. Results with alongfront and across-front winds show important differences.

Ekman boundary layer dynamics generates surface winds parallel (geostrophic) and perpendicular (ageostrophic) to the imposed pressure gradient $f\mathbf{U}_g$; f is the Coriolis parameter and $\mathbf{U}_g = (U_g, V_g)$ is the geostrophic wind vector. Typically, the ageostrophic surface wind is an order of magnitude smaller than the geostrophic wind (e.g., Wyngaard 2010). Thus in the present study a key difference between cases with alongfront winds and across-front winds is the magnitude of the wind component $\langle u\rangle$ blowing perpendicular to the SST isotherms. In the far field, away from the SST front, $-\langle\hat{u}\rangle/V_g = 0.17$ in the alongfront case compared to the across-front case where $\langle\hat{u}\rangle_{\text{acr}}/U_g = 0.85$. Thus, with (alongfront, across-front) winds horizontal advection $\langle u\rangle\langle\partial_x p\rangle$ near the SST front is (weak, strong).

A horizontal momentum balance written for the velocity perturbation from the far-field wind $u_p = \langle u - \hat{u}\rangle$ highlights the importance of horizontal advection, horizontal pressure gradients, and divergence of turbulence flux terms. Given a fixed value of $V_g = 10\,\text{m}\,\text{s}^{-1}$ horizontal pressure gradients $\langle\partial_x p\rangle$ play a significant role in maintaining the horizontal momentum budget with alongfront winds compared to across-front winds in S20 with $U_g = 10\,\text{m}\,\text{s}^{-1}$. With alongfront

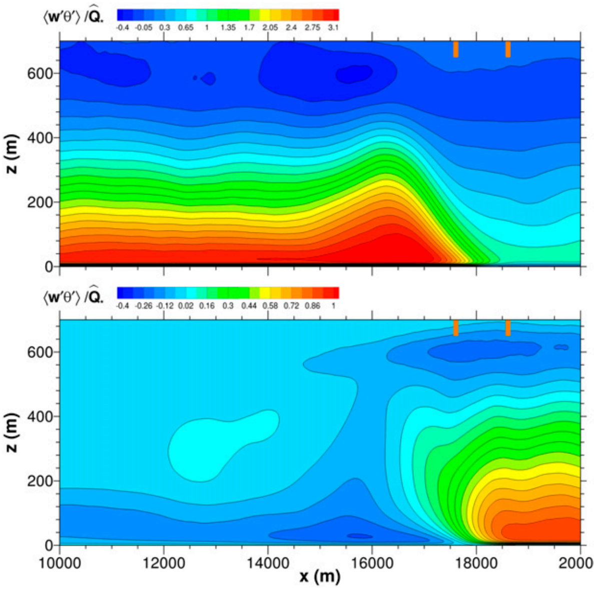

FIG. 17. Contours of normalized vertical temperature flux $\langle w'\theta'\rangle/\widehat{Q_*}$ for a (top) warm front and (bottom) cold front. The start and end locations of the SST change is shown by the orange vertical bars at the top of each panel. The ageostrophic wind u is from right to left.

winds above a warm front $-\langle\partial_x p\rangle$ is (positive, negative) near the (surface, boundary layer top). The sign of $\langle\partial_x p\rangle$ is reversed with cold front.

With weak surface winds $u < 0$, the MABL develops secondary circulation (SC) slightly left of the SST front; the SC are well organized and persistent. The SC rotate (clockwise, counterclockwise) for (warm, cold) front cases, respectively. The SC impact the surface momentum fluxes to a greater degree compared to similar simulations with across-front winds especially for stable SST fronts. The curl of the wind stress $\partial_x\langle\tau_y\rangle$ is larger than the divergence of the wind stress $\partial_x\langle\tau_x\rangle$. In the case of a cold front the surface wind is nearly reversed compared to the far-field value by the SC $\langle u\rangle \to 0$; hence the surface stress component $\tau_x \to 0$. With a warm front, the SC also generate significant momentum flux $-\langle u'w'\rangle$ compared to the total wind stress $\widehat{u_*^2}$; in the middle and upper MABL $-\langle u'w'\rangle/\widehat{u_*^2} \sim 0.85$. Cold fronts and SC, however, reduce the momentum flux in the MABL.

Parameter variations in SST show that warm and cold filaments, generated by pairs of warm-cold and cold-warm fronts separated by a finite distance, create pairs of opposing closed SC. Streamfunctions calculated from u_p show with (warm, cold) filaments there is a central (upwelling, downwelling) region. The SC pattern is shifted left of the surface temperature distribution. With weak surface winds the SC in the MABL are a cousin to the secondary circulations generated in free convective boundary layers over land (no mean wind) with surface heterogeneity (e.g., Krettenauer and Schumann 1992; Raasch and Harbusch 2001; Patton et al. 2005; Owinoh et al. 2005).

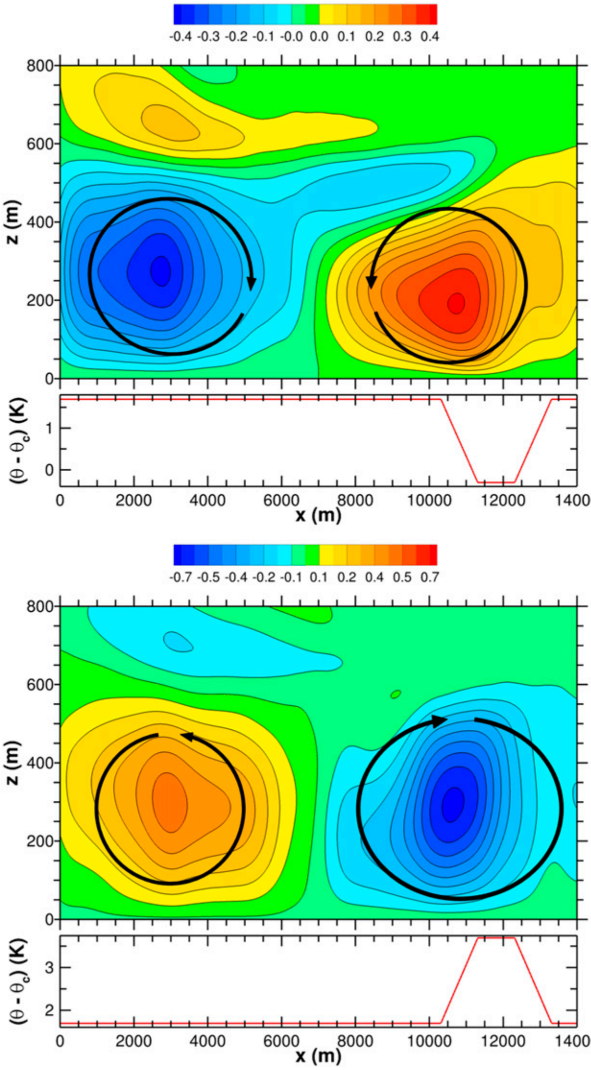

FIG. 18. Streamfunction ψ_p computed from the perturbation wind u_p normalized by $\widehat{z_i}/\widehat{u_*}$ for (top) cold and (bottom) warm filaments. The black stream traces indicate the average direction of the rotation. (bottom) The variation of the SST $\langle\theta - \theta_c\rangle$ with x. The far-field ageostrophic wind $\langle u\rangle$ is from right to left.

An important result from the present work emphasizes the importance of the magnitude and orientation of the surface-wind relative to the orientation of the SST isotherms. To establish correlations between boundary layer winds and SST, field observations in areas of oceanic fronts and internal boundary layers need to account for the magnitude and direction of the overlying MABL winds relative to the spatial variability in the SST (e.g., Wijesekera et al. 2016; Wang et al. 2018; Quinn et al. 2021; Shroyer et al. 2021). With alongfront winds above a warm front, the boundary layer entrainment flux $\langle w'\theta\rangle_e$ is nearly constant despite a factor of 3 increase in the surface temperature flux. The inversion layer and the standard assumptions for entrainment are disrupted by SC which has potential impacts for the prediction of low-level clouds and internal boundary layers in coastal regions. The linear

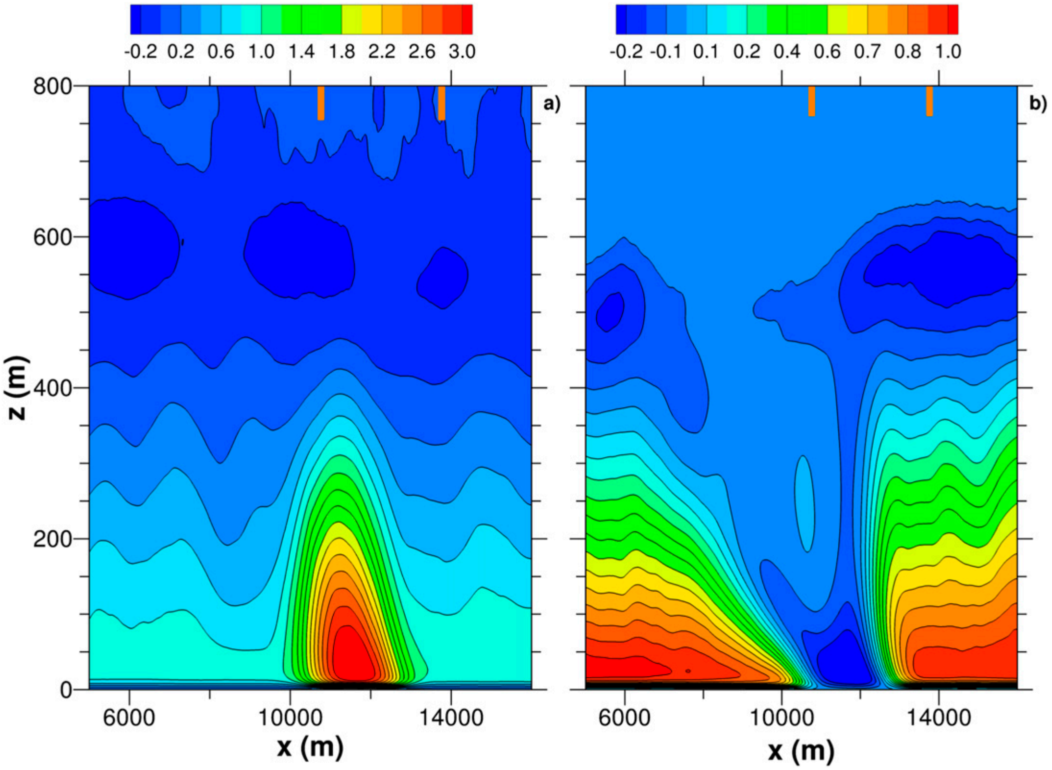

FIG. 19. Contours of average resolved temperature flux normalized by the far-field surface temperature flux $\langle w'\theta'\rangle/\widehat{Q_*}$ with alongfront winds for the SST filaments in Fig. 18. (a) Warm filament and (b) cold filament. The SST distribution is given in Fig. 18 and the color bar changes between the two panels. The cold filament impacts boundary layer structure and entrainment to a greater extent than the warm filament. The orange vertical bars mark the start and end of the filament.

momentum balance based on TTW needs to account for horizontal pressure gradients and nonlinear effects as discussed by McWilliams (2018). Warm and cold filaments develop pairs of closed cell SC. Cold filaments, which are common in the upper ocean, reduce the turbulence entrainment near the boundary layer top and thus can also potentially impact low-level cloud formation (Atkinson and Zhang 1996).

It is interesting to compare the response of the MABL and ocean boundary layer to surface SST (or density) variations. In the MABL, the Rossby number is large based on the perturbation velocities (u_p, υ_p) and the SC width, we estimate Ro ~ $\mathcal{O}(10)$. This is consistent with the Coriolis forcing being small and differs from oceanic fronts where $Ro \sim \mathcal{O}(1)$. The main MABL balance is a vertically sign-reversing (baroclinic) pressure gradient $\langle \partial_x p\rangle$ balanced by vertical flux divergence $\langle \partial_z u'w'\rangle$ and mean horizontal advection $\langle u\rangle \partial_x \langle u\rangle$. This is different from oceanic fronts in which $\langle \partial_x p\rangle$ usually does not change sign in z and the Coriolis forcing matters. Both MABL and oceanic regimes essentially involve vertical flux divergence, and both have w in the sense of upward flow on the warm/light side of an SST gradient and vice versa, but in the MABL the w circulation is displaced downwind, presumably by horizontal advection. This implies a conversion of potential energy to kinetic energy by the SC; we find $\langle w\rangle\langle \theta - \hat{\theta}\rangle > 0$ for all simulations (results not shown). This has the effect of locally restratifying (stabilizing) the MABL. Similar to ocean frontogenesis (Sullivan and McWilliams 2019; McWilliams 2020) in the MABL vertical momentum mixing plus horizontal gradients of surface buoyancy makes SC that have surface convergence and hence frontogenesis. With alongfront winds, the surface winds at the reference height $z = 10$ m show frontogenetic tendencies; we observe peaks in vertical vorticity $\langle \partial_x u\rangle/f$ with opposing horizontal gradients $\langle \partial_x u\rangle$ when averaged over a time period of 5400 s. The simulations and analysis by Wenegrat and Arthur (2018), assuming periodic sidewalls, suggest frontogenesis can potentially occur in the MABL with alongfront winds at long time scales.

The variation of wind stress presented here and in S20 is qualitatively consistent with large-scale satellite altimetry observations (e.g., Chelton et al. 2004). In LES, with across-front winds the wind stress divergence $\partial_x\langle \tau_x\rangle$ is large and well correlated with the change in SST. Meanwhile with alongfront winds wind stress curl $\partial_x\langle \tau_x\rangle$ is large and the results are consistent with observations. In LES the magnitude of the divergence and curl of wind stress varies with stability and the orientation of the near surface winds relative to the SST front. Recent work finds SST induced wind speed perturbations are surprisingly observed in the submesoscale regime of 1–10 km (Gaube et al. 2019; Shao et al. 2019), similar to the present LES experiments.

Acknowledgments. PPS and JCM were supported by the Office of Naval Research through the Physical Oceanography Program Awards N00014-17-1-2334 and N00014-18-1-2599 and by the National Oceanic and Atmospheric Administration Award NA19OAR4310378. HJSF was supported by the Office of Naval Research Award N00014-17-1-2334. PPS and EGP acknowledges support from the National Science Foundation and the Geophysical Turbulence Program at the National Center for Atmospheric Research. This research benefited greatly from computer resources provided by the Department of Defense High Performance Computing Modernization Program and NCAR's Computational and Information Systems Laboratory (doi:10.5065/D6RX99HX) sponsored by the National Science Foundation. The comments from three reviewers helped to improve the manuscript.

REFERENCES

Anderson, W., J. M. Barros, K. T. Christensen, and A. Awasthi, 2015: Numerical and experimental study of mechanisms responsible for turbulent secondary flows in boundary layer flows over spanwise heterogeneous roughness. *J. Fluid Mech.*, **768**, 316–347, https://doi.org/10.1017/jfm.2015.91.

Atkinson, B. W., and J. W. Zhang, 1996: Mesoscale shallow convection in the atmosphere. *Rev. Geophys.*, **34**, 403–431, https://doi.org/10.1029/96RG02623.

Chelton, D. B., M. G. Schlax, M. H. Frelich, and R. F. Miliff, 2004: Satellite measurements reveal persistent small-scale features in ocean winds. *Science*, **303**, 978–983, https://doi.org/10.1126/science.1091901.

Chen, W., M. L. Banner, E. J. Walsh, J. B. Jensen, and S. Lee, 2001: The Southern Ocean Waves Experiment. Part II: Sea surface response to wind speed and wind stress variations. *J. Atmos. Sci.*, **31**, 174–198, https://doi.org/10.1175/1520-0485(2001)031<0174:TSOWEP>2.0.CO;2.

Cronin, M. F., and Coauthors, 2019: Air-sea fluxes with a focus on heat and momentum. *Front. Mar. Sci.*, **6**, 4–30, https://doi.org/10.3389/fmars.2019.00430.

D'Asaro, E., 2014: Turbulence in the upper-ocean mixed layer. *Annu. Rev. Mar. Sci.*, **6**, 101–115, https://doi.org/10.1146/annurev-marine-010213-135138.

Deardorff, J. W., 1970: A numerical study of three-dimensional turbulent channel flow at large Reynolds numbers. *J. Fluid Mech.*, **41**, 453–480, https://doi.org/10.1017/S0022112070000691.

Edson, J., and Coauthors, 2007: The Coupled Boundary Layers and Air–Sea Transfer Experiment in Low Winds (CBLAST-Low). *Bull. Amer. Meteor. Soc.*, **88**, 341–356, https://doi.org/10.1175/BAMS-88-3-341.

Gaube, P., C. C. Chickadel, R. Branch, and A. Jessup, 2019: Satellite observations of SST-induced wind speed perturbation at the oceanic submesoscale. *Geophys. Res. Lett.*, **46**, 2690–2695, https://doi.org/10.1029/2018GL080807.

Gula, J., M. J. Molemaker, and J. C. McWilliams, 2014: Submesoscale cold filaments in the Gulf Stream. *J. Phys. Oceanogr.*, **44**, 2617–2643, https://doi.org/10.1175/JPO-D-14-0029.1.

Krettenauer, K., and U. Schumann, 1992: Numerical simulation of turbulent convection over wavy terrain. *J. Fluid Mech.*, **237**, 261–299, https://doi.org/10.1017/S0022112092003410.

Large, W. G., and S. Pond, 1981: Open ocean flux measurements in moderate to strong winds. *J. Phys. Oceanogr.*, **11**, 324–336, https://doi.org/10.1175/1520-0485(1981)011<0324:OOMFMI>2.0.CO;2.

Liang, J.-H., E. A. D'Asaro, C. L. McNeil, Y. Fan, R. R. Harcourt, S. R. Emerson, B. Yang, and P. P. Sullivan, 2020: Suppression of CO_2 outgassing by gas bubbles under a hurricane. *Geophys. Res. Lett.*, **47**, e2020GL090249, https://doi.org/10.1029/2020GL090249.

Lilly, D. K., 1986: The structure, energetics and propagation of rotating convective storms. Part I: Energy exchange with the mean flow. *J. Atmos. Sci.*, **43**, 113–125, https://doi.org/10.1175/1520-0469(1986)043<0113:TSEAPO>2.0.CO;2.

Manasseh, R., C.-Y. Ching, and H. J. S. Fernando, 1998: The transition from density-driven to wave-dominated isolated flows. *J. Fluid Mech.*, **361**, 253–274, https://doi.org/10.1017/S0022112098008775.

McWilliams, J. C., 2016: Submesoscale currents in the ocean. *Proc. Roy. Soc. London*, **472A**, 20160117, https://doi.org/10.1098/rspa.2016.0117.

——, 2018: Surface wave effects on submesoscale fronts and filaments. *J. Fluid Mech.*, **843**, 479–517, https://doi.org/10.1017/jfm.2018.158.

——, 2020: Oceanic frontogenesis. *Annu. Rev. Mar. Sci.*, **13**, 227–253, https://doi.org/10.1146/annurev-marine-032320-120725.

——, C.-H. Moeng, and P. P. Sullivan, 1999: Turbulent fluxes and coherent structures in marine boundary layers: Investigations by large-eddy simulation. *Air-Sea Exchange: Physics, Chemistry, Dynamics, and Statistics*, G. Geernaert, Ed., Kluwer Academic Publishers, 507–538.

——, F. Colas, and M. J. Molemaker, 2009: Cold filamentary intensification and oceanic surface convergence lines. *Geophys. Res. Lett.*, **36**, L18602, https://doi.org/10.1029/2009GL039402.

——, J. Gula, M. J. Molemaker, L. Renault, and A. F. Shchepetkin, 2015: Filament frontogenesis by boundary layer turbulence. *J. Phys. Oceanogr.*, **45**, 1988–2005, https://doi.org/10.1175/JPO-D-14-0211.1.

Miller, S. T. K., B. D. Keim, R. W. Talbot, and H. Mao, 2003: Sea breeze: Structure, forecasting, and impacts. *Rev. Geophys.*, **41**, 1011–1042, https://doi.org/10.1029/2003RG000124.

Moeng, C.-H., 1984: A large-eddy simulation model for the study of planetary boundary-layer turbulence. *J. Atmos. Sci.*, **41**, 2052–2062, https://doi.org/10.1175/1520-0469(1984)041<2052:ALESMF>2.0.CO;2.

——, and J. C. Wyngaard, 1986: An analysis of closures for pressure-scalar convariances in the convective boundary layer. *J. Atmos. Sci.*, **43**, 2499–2513, https://doi.org/10.1175/1520-0469(1986)043<2499:AAOCFP>2.0.CO;2.

——, and P. P. Sullivan, 1994: A comparison of shear and buoyancy driven planetary-boundary-layer flows. *J. Atmos. Sci.*, **51**, 999–1022, https://doi.org/10.1175/1520-0469(1994)051<0999:ACOSAB>2.0.CO;2.

——, and ——, 2015: Large-eddy simulation. *Encyclopedia of Atmospheric Sciences*, 2nd ed. G. R. North, F. Zhang, and J. Pyle, Eds., Vol. 4, Academic Press, 232–240.

——, J. C. McWilliams, R. Rotunno, P. P. Sullivan, and J. Weil, 2004: Investigating 2D modeling of atmospheric convection in the PBL. *J. Atmos. Sci.*, **61**, 889–903, https://doi.org/10.1175/1520-0469(2004)061<0889:IDMOAC>2.0.CO;2.

Nordström, J., N. Nordin, and D. Henningson, 1999: The fringe region technique and the Fourier method used in the direct numerical simulation of spatially evolving viscous flows. *SIAM J. Sci. Comput.*, **20**, 1365–1393, https://doi.org/10.1137/S1064827596310251.

Owinoh, A., J. Hunt, A. Orr, P. Clark, R. Klein, H. Fernando, and F. Nieuwstadt, 2005: Effects of changing surface heat flux on atmospheric boundary-layer flow over flat terrain.

Bound.-Layer Meteor., **116**, 331–361, https://doi.org/10.1007/s10546-004-2819-z.

Patton, E. G., P. P. Sullivan, and C.-H. Moeng, 2005: The influence of idealized heterogeneity on wet and dry planetary boundary layers coupled to the land surface. *J. Atmos. Sci.*, **62**, 2078–2097, https://doi.org/10.1175/JAS3465.1.

——, ——, R. H. Shaw, J. J. Finnigan, and J. C. Weil, 2016: Atmospheric stability influences on coupled boundary layer and canopy turbulence. *J. Atmos. Sci.*, **73**, 1621–1647, https://doi.org/10.1175/JAS-D-15-0068.1.

Pope, S. B., 2000: *Turbulent Flows.* Cambridge University Press, 771 pp.

Quinn, P. K., and Coauthors, 2021: Measurements from the RV *Ronald H. Brown* and related platforms as part of the Atlantic Tradewind Ocean-Atmosphere Mesoscale Interaction Campaign (ATOMIC). *Earth Syst. Sci. Data*, **13**, 1759–1790, https://doi.org/10.5194/essd-13-1759-2021.

Raasch, S., and G. Harbusch, 2001: An analysis of secondary circulations and their effects caused by small-scale surface inhomogeneities using large-eddy simulation. *Bound.-Layer Meteor.*, **101**, 31–59, https://doi.org/10.1023/A:1019297504109.

Renault, L., P. Marchesiello, S. Masson, and J. C. McWilliams, 2019: Remarkable control of western boundary currents by eddy killing, a mechanical air-sea coupling process. *Geophys. Res. Lett.*, **46**, 2743–2751, https://doi.org/10.1029/2018GL081211.

Schmidt, H., and U. Schumann, 1989: Coherent structure of the convective boundary layer derived from large-eddy simulations. *J. Fluid Mech.*, **200**, 511–562, https://doi.org/10.1017/S0022112089000753.

Seo, H., A. J. Miller, and J. R. Norris, 2016: Eddy–wind interaction in the California Current System: Dynamics and impacts. *J. Phys. Oceanogr.*, **46**, 439–459, https://doi.org/10.1175/JPO-D-15-0086.1.

Shao, M., and Coauthors, 2019: The variability of winds and fluxes observed near submeoscale fronts. *J. Geophys. Res. Oceans*, **124**, 7756–7780, https://doi.org/10.1029/2019JC015236.

Shroyer, E., and Coauthors, 2021: Bay of Bengal intraseasonal oscillations and the 2018 monsoon onset. *Bull. Amer. Meteor. Soc.*, https://doi.org/10.1175/BAMS-D-20-0113.1, in press.

Skyllingstad, E. D., S. P. de Szoeke, and L. W. O'Neill, 2019: Modeling the transient response of tropical convection to mesoscale SST variations. *J. Atmos. Sci.*, **76**, 1227–1244, https://doi.org/10.1175/JAS-D-18-0079.1.

Small, R. J., and Coauthors, 2008: Air-sea interaction over ocean fronts and eddies. *Dyn. Atmos. Oceans*, **45**, 274–319, https://doi.org/10.1016/j.dynatmoce.2008.01.001.

Spalart, P. R., and J. H. Watmuff, 1993: Experimental and numerical study of a turbulent boundary layer with pressure gradients. *J. Fluid Mech.*, **249**, 337–371, https://doi.org/10.1017/S002211209300120X.

Stevens, B., and Coauthors, 2021: EUREC^{4}A. *Earth Syst. Sci. Data*, **13**, 4067–4119, https://doi.org/10.5194/essd-13-4067-2021.

Sullivan, P. P., and J. C. McWilliams, 2010: Dynamics of winds and currents coupled to surface waves. *Annu. Rev. Fluid Mech.*, **42**, 19–42, https://doi.org/10.1146/annurev-fluid-121108-145541.

——, and E. G. Patton, 2011: The effect of mesh resolution on convective boundary-layer statistics and structures generated by large-eddy simulation. *J. Atmos. Sci.*, **68**, 2395–2415, https://doi.org/10.1175/JAS-D-10-05010.1.

——, and J. C. McWilliams, 2018: Frontogenesis and frontal arrest of a dense filament in the oceanic surface boundary layer. *J. Fluid Mech.*, **837**, 341–380, https://doi.org/10.1017/jfm.2017.833.

——, and ——, 2019: Langmuir turbulence and filament frontogenesis in the oceanic surface boundary layer. *J. Fluid Mech.*, **879**, 512–553, https://doi.org/10.1017/jfm.2019.655.

——, ——, and C.-H. Moeng, 1994: A subgrid-scale model for large-eddy simulation of planetary boundary-layer flows. *Bound.-Layer Meteor.*, **71**, 247–276, https://doi.org/10.1007/BF00713741.

——, ——, and ——, 1996: A grid nesting method for large-eddy simulation of planetary boundary layer flows. *Bound.-Layer Meteor.*, **80**, 167–202, https://doi.org/10.1007/BF00119016.

——, C.-H. Moeng, B. Stevens, D. H. Lenschow, and S. D. Mayor, 1998: Structure of the entrainment zone capping the convective atmospheric boundary layer. *J. Atmos. Sci.*, **55**, 3042–3064, https://doi.org/10.1175/1520-0469(1998)055<3042:SOTEZC>2.0.CO;2.

——, J. C. McWilliams, and E. G. Patton, 2014: Large-eddy simulation of marine atmospheric boundary layers above a spectrum of moving waves. *J. Atmos. Sci.*, **71**, 4001–4027, https://doi.org/10.1175/JAS-D-14-0095.1.

——, ——, J. C. Weil, E. G. Patton, and H. J. S. Fernando, 2020: Marine atmospheric boundary layers above heterogeneous SST: Across-front winds. *J. Atmos. Sci.*, **77**, 4251–4275, https://doi.org/10.1175/JAS-D-20-0062.1.

Sykes, R. I., and D. S. Henn, 1989: Large-eddy simulation of turbulent sheared convection. *J. Atmos. Sci.*, **46**, 1106–1118, https://doi.org/10.1175/1520-0469(1989)046<1106:LESOTS>2.0.CO;2.

Taylor, J. R., and R. Ferrari, 2010: Buoyancy and wind-driven convection at mixed layer density fronts. *J. Phys. Oceanogr.*, **40**, 1222–1242, https://doi.org/10.1175/2010JPO4365.1.

Thomas, L. N., and C. Lee, 2005: Intensification of ocean fronts by down-front winds. *J. Phys. Oceanogr.*, **35**, 1086–1102, https://doi.org/10.1175/JPO2737.1.

Wang, Q., and Coauthors, 2018: CASPER: Coupled Air–Sea Processes and Electromagnetic Ducting Research. *Bull. Amer. Meteor. Soc.*, **99**, 1449–1471, https://doi.org/10.1175/BAMS-D-16-0046.1.

Wenegrat, J. O., and R. S. Arthur, 2018: Response of the atmospheric boundary layer to submesoscale sea-surface temperature fronts. *Geophys. Res. Lett.*, **45**, 13 505–13 512, https://doi.org/10.1029/2018GL081034.

Wijesekera, H. W., and Coauthors, 2016: ASIRI: An ocean–atmosphere initiative for Bay of Bengal. *Bull. Amer. Meteor. Soc.*, **97**, 1859–1884, https://doi.org/10.1175/BAMS-D-14-00197.1.

Willis, G. E., and J. W. Deardorff, 1976: A laboratory model of diffusion into the convective planetary boundary layer. *Quart. J. Roy. Meteor. Soc.*, **102**, 427–445, https://doi.org/10.1002/qj.49710243212.

Wyngaard, J. C., 2010: *Turbulence in the Atmosphere.* Cambridge University Press, 393 pp.